

Supporting Information

Mechanisms and Active Sites for C-O Bond Rupture within 2-Methyltetrahydrofuran over Ni, Ni₁₂P₅, and Ni₂P Catalysts

Megan E. Witzke,¹ Abdulrahman Almithn,² Christian L. Coonrod,¹ David D. Hibbitts,² and David W. Flaherty^{1,*}

¹Department of Chemical and Biomolecular Engineering
University of Illinois Urbana-Champaign, Urbana, IL 61801

²Department of Chemical Engineering
University of Florida, Gainesville, FL 32611

*Corresponding Authors

D. Flaherty: dwflhrt@illinois.edu

D. Hibbitts: hibbitts@ufl.edu

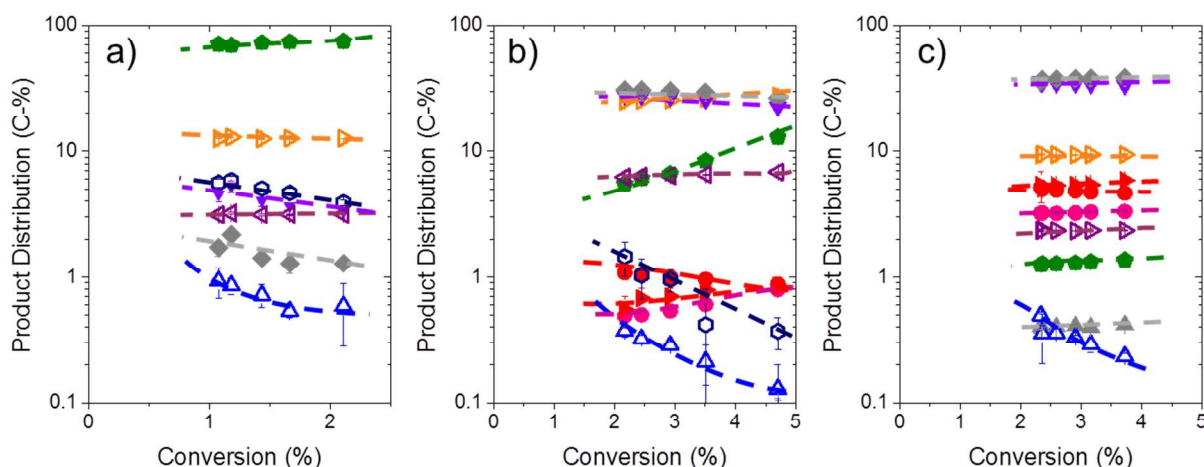


Figure S1. Selectivities towards primary products of C-O bond rupture including pentanal (Δ) and 2-penten-4-one (\bullet); and secondary products formed by subsequent C-C or C-O bond rupture or hydrogenations including methane (\bullet), n-butane (\triangleright), n-pentane (\blacklozenge), pentene (\blacktriangle), 2-penten-4-ol (\blacktriangleright), 2-pentanone (\blacktriangledown), 2-pentanol (\blacklozenge), 1-pentanol (\circ), and carbon monoxide (\blacktriangledown) over SiO_2 -supported (a) 12 nm Ni_2P , (b) 5 nm Ni_{12}P_5 , (c) and 4 nm Ni at 5 kPa MTHF, 1 MPa H_2 , and 543 K. Remaining products sum to less than 1% of product distribution. Lines are drawn to guide the eye.

Table S1. Range of residence times and H_2 flow rates for data represented in Figures 1 and S1

Catalyst	Residence Times $\text{s} \cdot \text{mol CO}_{\text{ads}} \cdot (\text{mol MTHF})^{-1}$	H_2 Flow Rates sccm
12 nm Ni_2P	2.4 – 6.1	194 - 484
19 nm Ni_{12}P_5	0.092 – 5.2 ^a	48 - 484
5 nm Ni_{12}P_5	0.89 - 2.2	194 - 484
4 nm Ni	0.044 - 0.11	194 - 484

^aSeparate experiments with catalyst material ranging from 25 – 490 mg were used. SiO_2 was added to keep the volume of the bed constant at 1.4 cm^3 or at total mass of 500 mg of SiO_2 and SiO_2 supported catalyst.

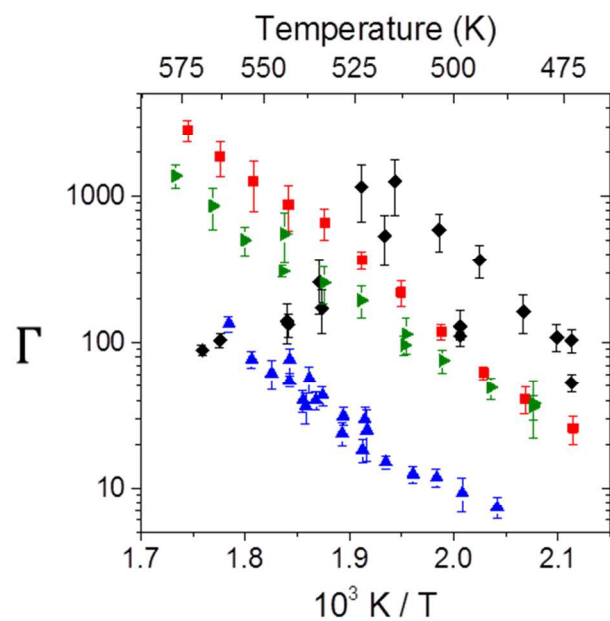


Figure S2. The ratio of initial C-O to C-C bond rupture rates (Γ) for 4 nm Ni (\blacklozenge), 5 nm $Ni_{12}P_5$ (\blacktriangleright), 19 nm $Ni_{12}P_5$ (\blacksquare), and 12 nm Ni_2P (\blacktriangle) at 1 MPa H_2 , and 5 kPa MTHF.

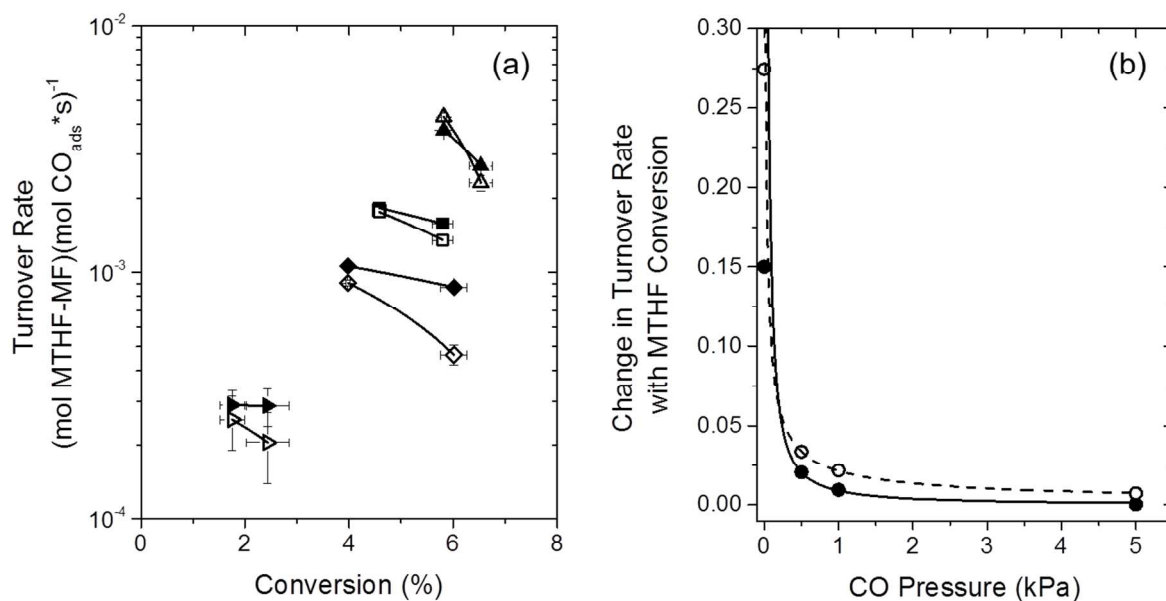


Figure S3. (a) Rates of consumption of the MTHF-MF reactant pool to form pentanal and subsequent ³C-O bond rupture products (hollow), and 2-penten-4-one and subsequent ²C-O bond rupture products (filled) indicated in Scheme 1 with conversion at different pressures of co-fed CO (0 kPa, ▲; 0.5 kPa, ■; 1 kPa, ◆; 5 kPa, ►) during reactions of MTHF over silica supported 5 nm Ni₁₂P₅ in 5 kPa MTHF and 1 MPa H₂ at 543 K. (b) The absolute value of slope from the linear fit in (a) as a function of co-fed CO pressure. Trendlines in (b) are intended to guide the eye

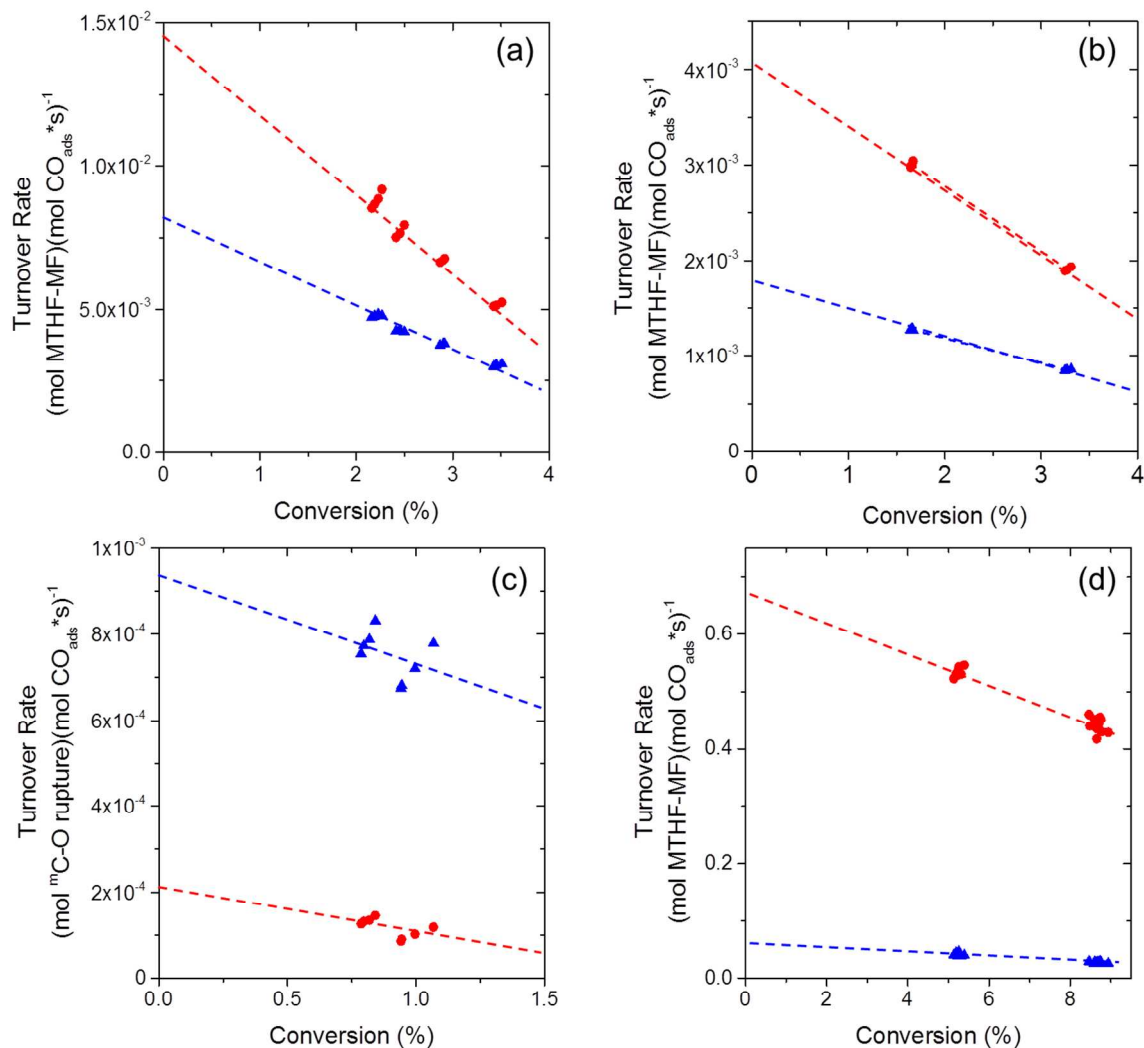


Figure S4. Measured rates of consumption of the MTHF-MF reactant pool to form pentanal and subsequent ³C-O bond rupture products (r_{3C-O} , ▲), and 2-penten-4-one and subsequent ²C-O bond rupture products (r_{2C-O} , ●) indicated in Scheme 1 as a function of MTHF conversion over SiO₂ supported (a) 5 nm Ni₁₂P₅, (b) 19 nm Ni₁₂P₅, (c) 12 nm Ni₂P, (d) and 4 nm Ni at 5 kPa MTHF, 1 MPa H₂, and 543 K.

The decrease in rates with increasing conversion is attributed to product inhibition, particularly CO. Reported rates are extrapolated to infinite space velocities or 0% conversion, or the intercept as determined from a linear regression unless CO or NH₃ are co-fed with the reactants. The standard deviation of the reported rate is based on the standard deviation of the intercept value. Section S5 gives a full description of error analysis and propagation.

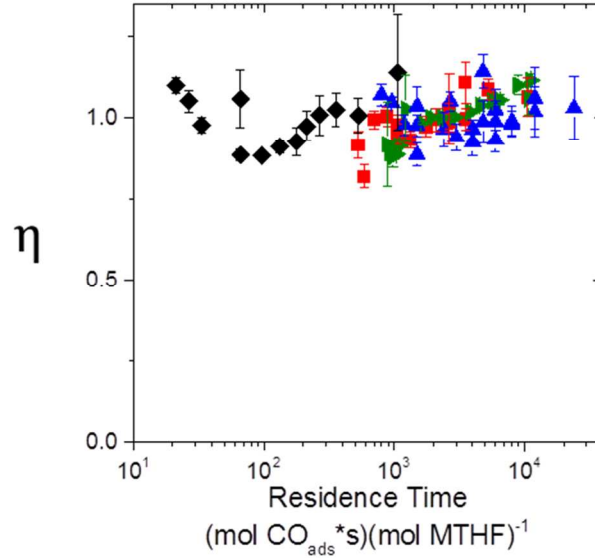


Figure S5. The approach to equilibrium (η) over for 4 nm Ni (◆, 2.5 kPa CO, 500 kPa H₂), 5 nm Ni₁₂P₅ (▶, 1 kPa CO, 250 kPa H₂), 19 nm Ni₁₂P₅ (■, 2.5 kPa CO, 500 kPa H₂), and 12 nm Ni₂P (▲, 2.5 kPa CO, 500 kPa H₂) during MTHF dependence experiments (1-50 kPa MTHF) at 543K.

Additional details for calculating the approach to equilibrium are shown in Section S4.

S1. Calculated Parameters for First Order Langmuir-Hinshelwood Competitive Adsorption Model from MTHF Dependence

Measured turnover rates for initial C-O bond rupture as a function of MTHF pressure are fit to a Langmuir-Hinshelwood equation:

$$\frac{r_{m_{C-O}}}{[L]} = \frac{k * K * [MTHF]^n}{K_{CO}[CO] + K * [MTHF]^n} \quad (S1)$$

Where k is the apparent rate constant for C-O bond rupture, K is the group of equilibrium constants for elementary steps leading to the formation of the MTHF derived most abundant surface intermediate (MASI), K_{CO} is the adsorption equilibrium constant for CO, n is the number MTHF molecules present in the transition state for C-O bond rupture, and [CO] and [MTHF] are the partial pressures of CO and MTHF, respectively. Rearranging Equation S1 gives the following equation,

$$\frac{r_{m_{C-O}}}{[L]} = \frac{k * \frac{K}{K_{CO}[CO]} * [MTHF]^n}{1 + \frac{K}{K_{CO}[CO]} * [MTHF]^n} \quad (S2)$$

which was used to fit k and $\frac{K}{K_{CO}[CO]}$ separately using Origin Pro while n was constrained to be 1 under the assumption that C-O bond rupture in MTHF does not require two MTHF molecules to interact prior to the transition state.

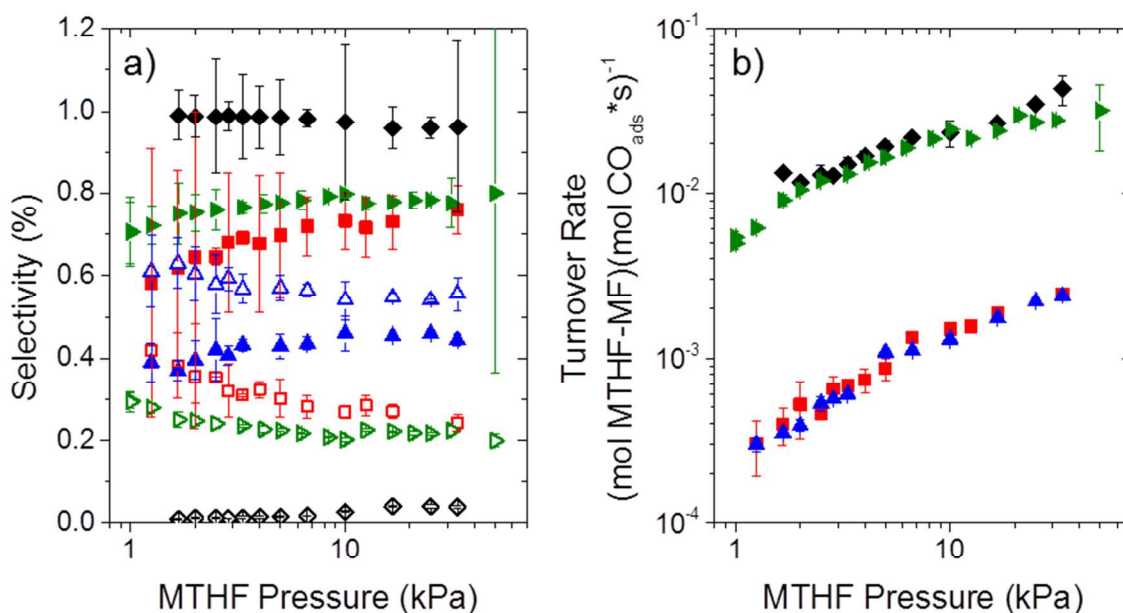


Figure S6. Changes in selectivity (a) for formation of pentanal and subsequent ³C-O bond rupture products (hollow), and 2-penten-4-one and subsequent ²C-O bond rupture products (filled) indicated in Scheme 1 and changes in the rate of consumption of the MTHF-MF reactant pool towards ^mC-O bond rupture products (b) as functions of MTHF pressure in the presence of CO over 4 nm Ni (◆, 2.5 kPa CO, 500 kPa H₂), 5 nm Ni₁₂P₅ (▶, 1 kPa CO, 250 kPa H₂), 19 nm Ni₁₂P₅ (■, 2.5 kPa CO, 500 kPa H₂), and 12 nm Ni₂P (▲, 2.5 kPa CO, 500 kPa H₂) at 543 K.

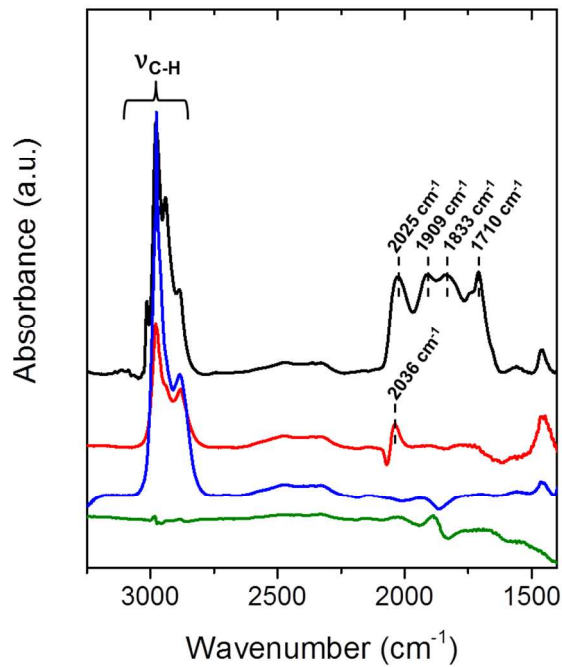


Figure S7. *In situ* FTIR spectra of surface species formed during reaction of MTHF with H₂ on silica supported 4 nm Ni (black), 10 nm Ni₁₂P₅ (red), and 12 nm Ni₂P (blue) catalysts and bare SiO₂ (green) (5 kPa MTHF, 81 kPa H₂, 15 kPa He, 543 K). Gas phase contributions are subtracted.

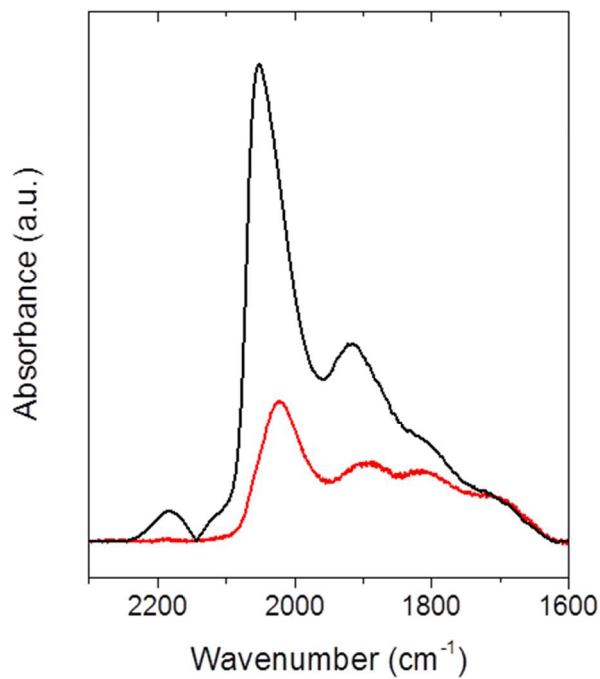


Figure S8. FTIR spectra of CO surface species formed while flowing 1% CO in He (black) and after sweeping with 30 cm³ min⁻¹ for 10 min (red) over silica supported 4 nm Ni clusters at 543 K.

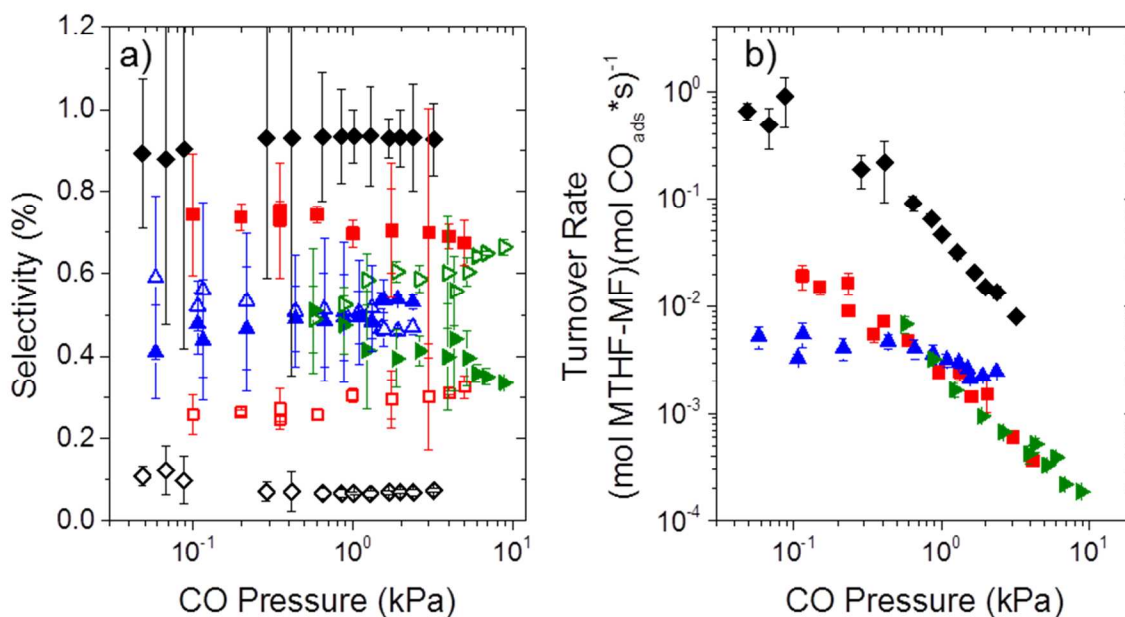


Figure S9. Changes in selectivity (a) for formation of pentanal and subsequent ³C-O bond rupture products (hollow), and 2-penten-4-one and subsequent ²C-O bond rupture products (filled) indicated in Scheme 1 and changes in the rate of consumption of the MTHF-MF reactant pool towards ^mC-O bond rupture products (b) as functions of CO pressure over 4 nm Ni (◆, 0.5 MPa H₂), 5 nm-Ni₁₂P₅ (▶, 1 MPa H₂), 19 nm-Ni₁₂P₅ (■, 0.5 MPa H₂), and Ni₂P (▲, 0.25 MPa H₂) in 5 kPa MTHF at 543 K.

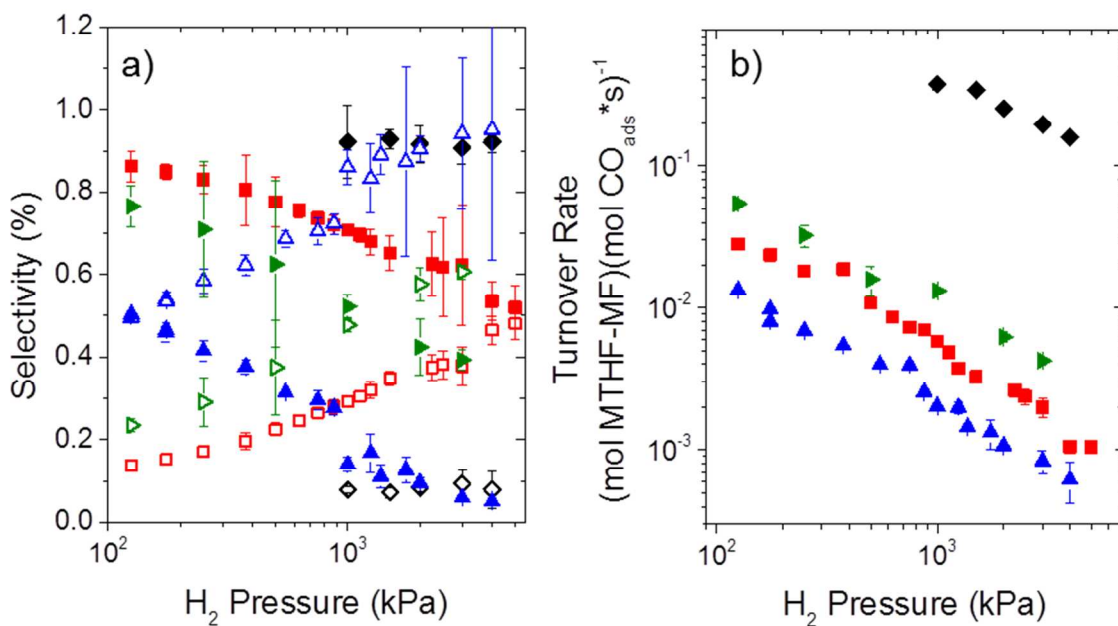


Figure S10. Changes in selectivity (a) for formation of pentanal and subsequent ³C-O bond rupture products (hollow), and 2-penten-4-one and subsequent ²C-O bond rupture products (filled) indicated in Scheme 1 and changes in the rate of consumption of the MTHF-MF reactant pool towards ^mC-O bond rupture products (b) as functions of H₂ pressure over 4 nm Ni (◆), 5 nm Ni₁₂P₅ (▶), 19 nm Ni₁₂P₅ (■), and 12 nm Ni₂P (▲) in 5 kPa MTHF at 543 K.

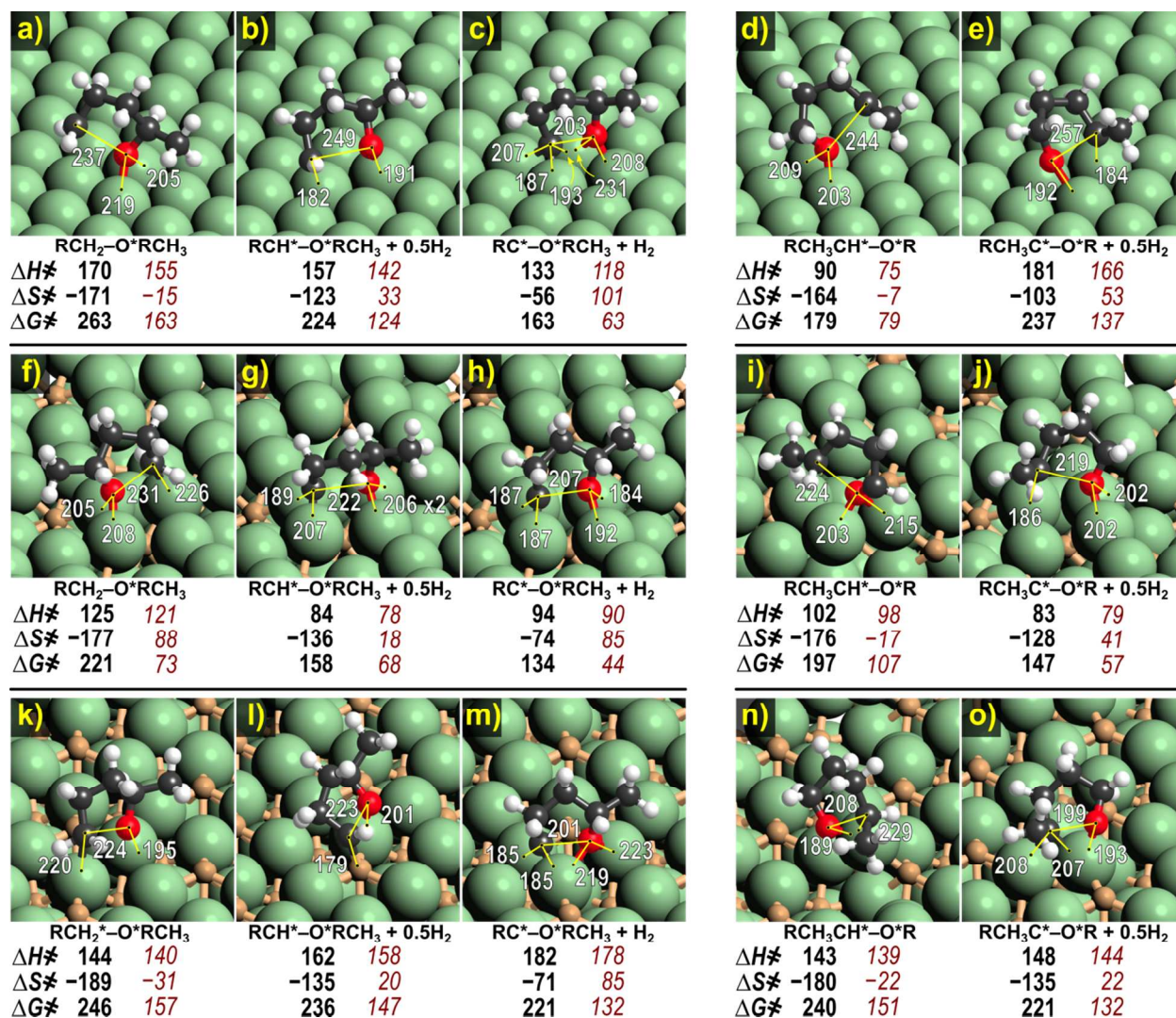


Figure S11. Transition-state structures on Ni(111) (a-e), Ni₁₂P₅(001) (f-j) and Ni₂P(001) (k-o) for ²C–O (a-c, f-h, k-m) and ³C–O (d-e, i-j, n-o) bond rupture dehydrogenated to varying degrees (i.e., removal of 0, 1, or 2 H-atoms from the ^mC in MTHF) at 543 K. Shown beneath each image are ΔH^\ddagger (kJ mol⁻¹), ΔS^\ddagger (J mol⁻¹ K⁻¹), ΔG^\ddagger (kJ mol⁻¹) for forming each state from a bare surface (black, bold) and from C₅H₈O*-covered surface (red, italic) as described in Figures 6, 7, S12 and S14. ²C–O and ³C–O bond rupture transition states on Ni₂P(001) are bound to Ni three-fold hollows (M₃), while ²C–O and ³C–O bond rupture transition states on Ni₁₂P₅(001) are bound to the four-fold Ni hollows (M_{4a}) as described in Figure 8. Important bond distances are shown in (pm). (O, red; C, black; H, white; P, orange; Ni, green).

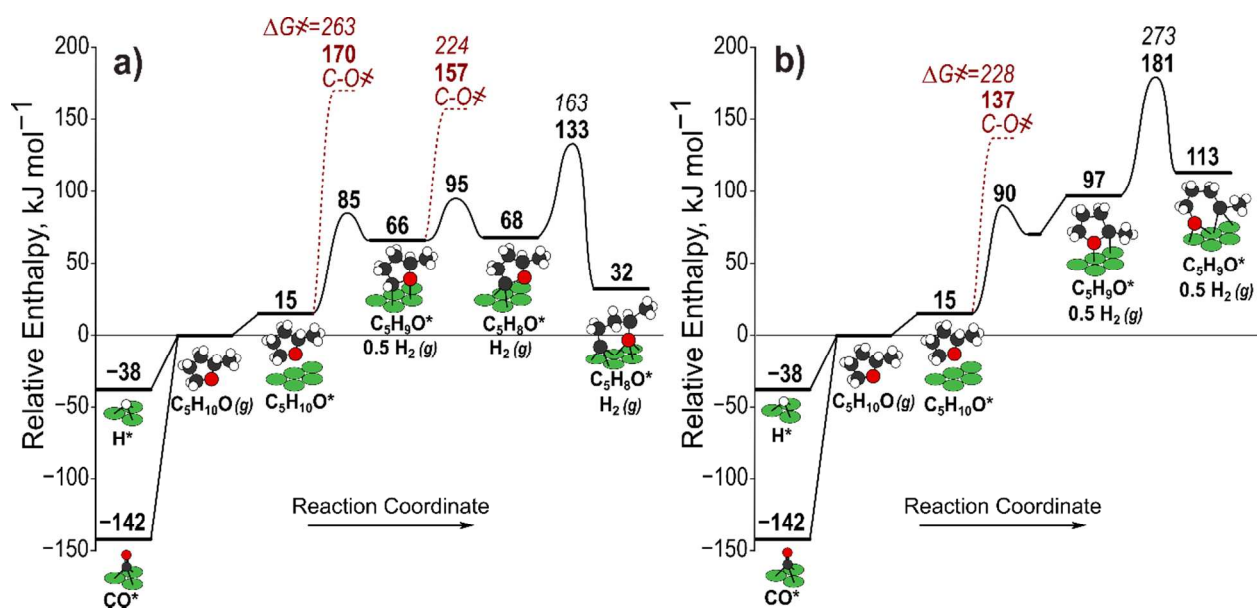


Figure S12. Reaction coordinate diagram for changes in enthalpy in elementary steps that form the transition state for ²C-O (a) and ³C-O (b) bond rupture in MTHF on a Ni(111) surface at 543 K (O: red; C: black; H: white; Ni: green).

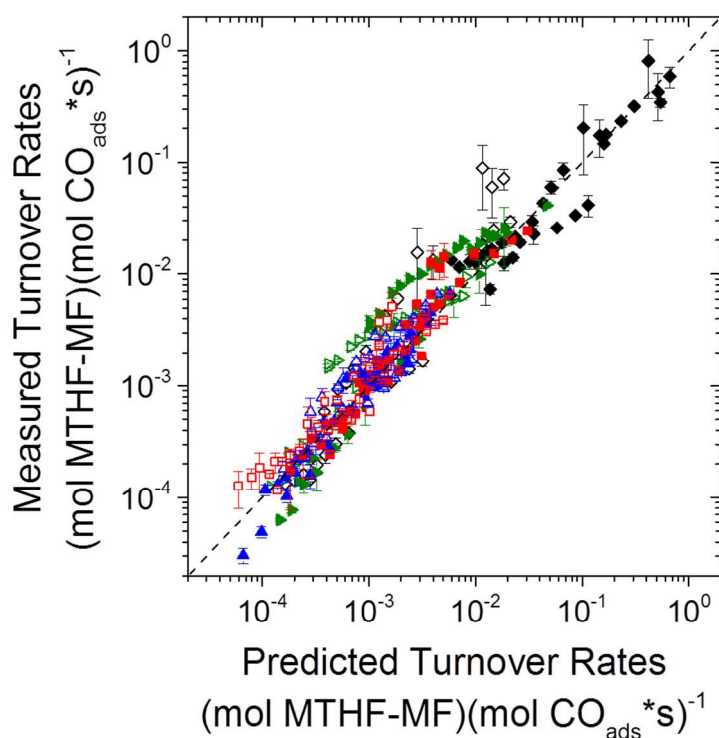


Figure S13. Parity plot of experimentally measured rates of consumption of the MTHF-MF reactant pool to form pentanal and subsequent $^3\text{C-O}$ bond rupture products (hollow), and 2-penten-4-one and subsequent $^2\text{C-O}$ bond rupture products (filled) indicated in Scheme 1 compared with predicted rates based on Equations 6a and 6b on 4 nm Ni (◆), 5 nm Ni_{12}P_5 (▶), 19 nm Ni_{12}P_5 (■), and 12 nm Ni_2P (▲) at 543 K. Trend lines reflects the ideal fit to the data.

Measured rates shown in Figure S13 include all of the reported rates for 4 nm Ni, 5 nm Ni_{12}P_5 , 19 nm Ni_{12}P_5 , and 12 nm Ni_2P across a wide range of conditions described in Figures 3-5. Regressions of independent rate measurements as a function of $[\text{MTHF}]$, $[\text{H}_2]$, and $[\text{CO}]$ provide values for rate constants (Table S2), which were then used to calculate the predicted rates shown in Figure S13.

Table S2. Regressed rate constants at 543 K described in Scheme 2, and Equations 6a and 6b extracted from measured rate data shown in Figures 3-5 and used to calculate the predicted rates in Figure S13.

Rate Constants		Ni	5 nm Ni_{12}P_5	19 nm Ni_{12}P_5	12 nm Ni_2P
K_0	$k\text{Pa}^{-1}$	3.5×10^{-5}	1053	2.8	2865
K_1	$k\text{Pa}^{-1}$	0.45	1882	56	193
K_{CO}	$k\text{Pa}^{-1}$	181	51004	1208	1591
$k_{3b} * K_{2b} * K_1 / K_0^{0.5}$	$(\text{mol MTHF-MF})(k\text{Pa} * \text{mol CO}_{\text{ads}} * \text{s})^{-1}$	1.0	349	3.3	16
$k_{4a} * K_{3a} * K_{2a} * K_1 / K_0$	$(\text{mol MTHF-MF})(\text{mol CO}_{\text{ads}} * \text{s})^{-1}$	804	13477	229	230

Table S3. DFT-calculated adsorbates binding energies ΔH_{ads} (kJ mol^{-1}) and their most stable adsorption modes on Ni(111), Ni₁₂P₅(001) and Ni₂P(001) at 543 K.

	C ₅ H ₁₀ O*			CO*				H*			NH ₃ *		
	Ni Vertical	Ni ₂ P Parallel	Ni ₁₂ P ₅ Parallel	Ni M ₃	Ni ₂ P M ₁	Ni ₁₂ P ₅ M _{4a} M _{4b}		Ni M ₃	Ni ₂ P M ₃	Ni ₁₂ P ₅ M _{4b}	Ni M ₁	Ni ₂ P M ₁	Ni ₁₂ P ₅ M ₁
RPBE	15	4	4	-142	-104	-69	-204	-38	-10	-77	-38	-52	-73
optB88-vdW	-75	-46	-54	-187	-143	-105	-242	-50	-24	-85	-86	-102	-121
optB86b-vdW	-93	-45	-53	-203	-148	-121	-264	-56	-24	-93	-94	-104	-128
RPBE-D3BJ	-136	-35	-41	-209	-148	-132	-275	-60	-20	-103	-98	-104	-131
vdW-DF2	-61	-41	-49	-122	-111	-50	-157	-27	-84	-61	-61	-114	-86

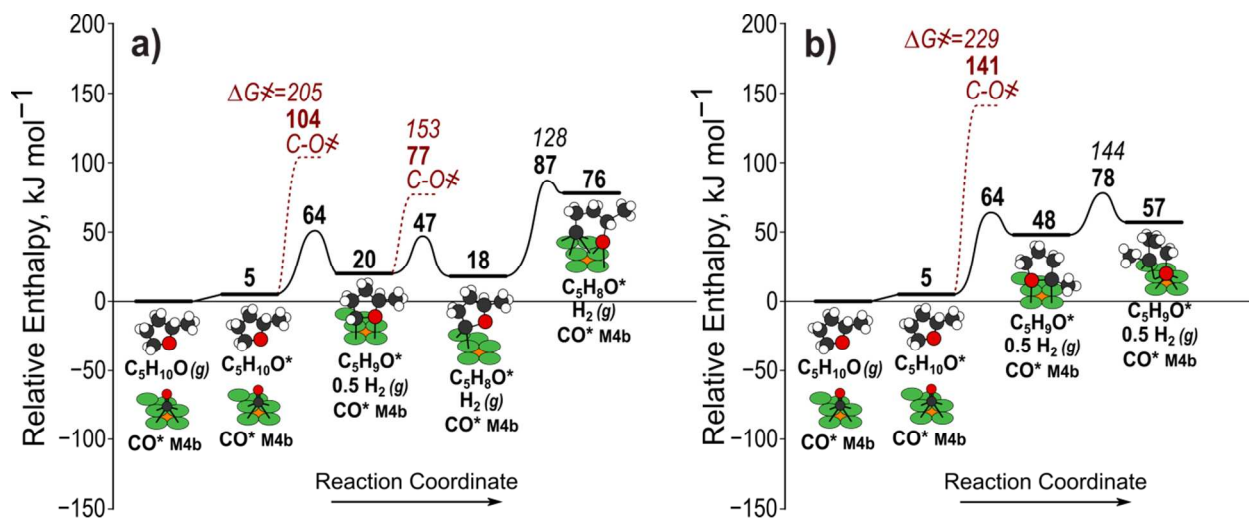


Figure S14. Reaction coordinate diagram for changes in enthalpy in elementary steps that form the transition state for ^2C-O (a) and ^3C-O (b) bond rupture in MTHF on a $Ni_{12}P_5(001)$ surface at 543 K with a spectating CO^* on the $M4_b$ site (O: red; C: black; H: white; P: orange; Ni: green).

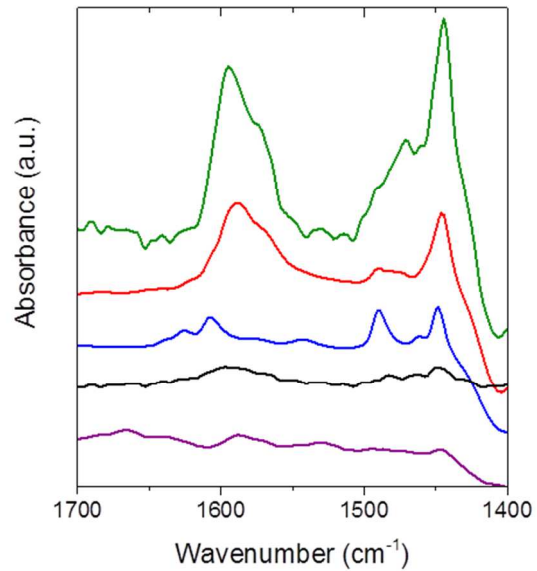


Figure S15. *In situ* FTIR spectra of surface species formed during reaction of MTHF and H₂ with co-fed pyridine on SiO₂-supported 4 nm Ni (black), 5 nm Ni₁₂P₅ (green), 19 nm Ni₁₂P₅ (red), 12 nm Ni₂P (blue) and bare SiO₂ (purple) at 1kPa pyridine, 5 kPa, 80 kPa H₂, 15 kPa He, 543 K. Gas phase contributions are subtracted.

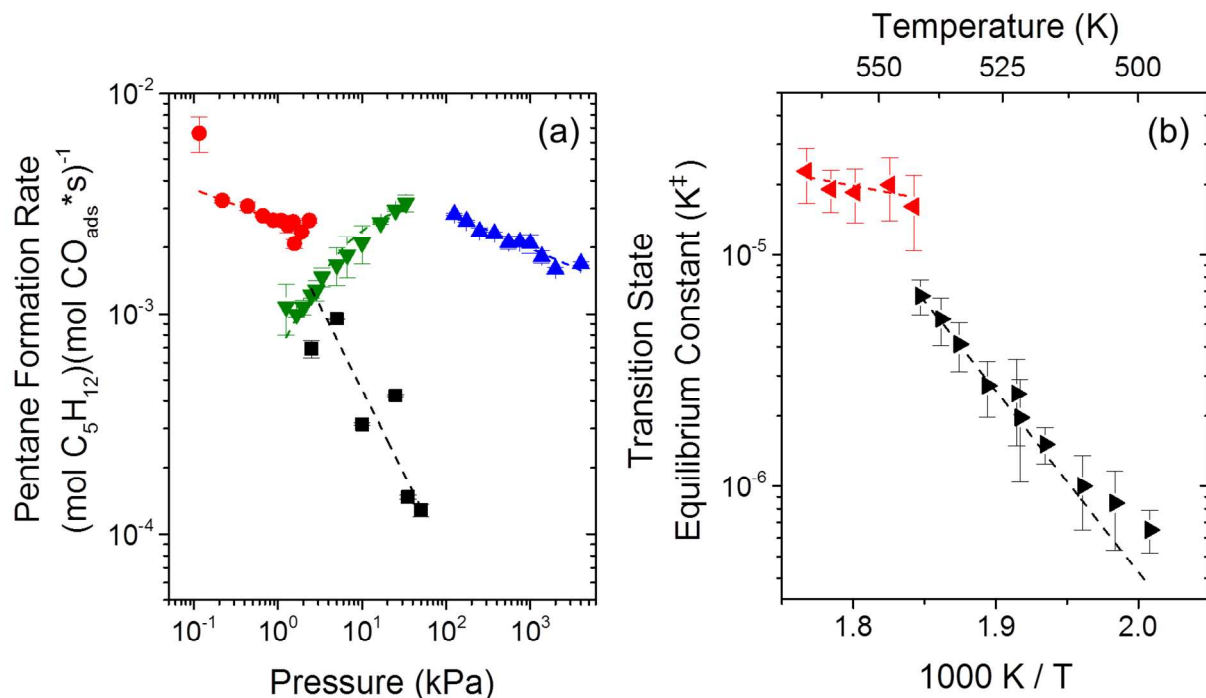


Figure S16. a) Change in pentane formation rates over SiO₂ supported 12 nm Ni₂P as a function of [MTHF] (∇ , 0.5 MPa H₂), [H₂] (\blacktriangle , 5 kPa MTHF), [CO] (\bullet , 5 kPa MTHF, 0.25 MPa H₂), and [NH₃] (\blacksquare , 5 kPa MTHF, 0.25 MPa H₂) at 543 K. Trend lines (---) for [H₂], [NH₃], and [CO] indicate power law fits and the trend line for [MTHF] reflects a fit to an inhibited unimolecular, Langmuir Hinshelwood expression. b) Transition state equilibrium constant (K^\ddagger) for pentane formation as a function of inverse temperature on SiO₂ supported 12 nm Ni₂P at 0.125 MPa H₂ (\blacktriangleleft), and 1 MPa H₂ (\blacktriangleright) in 5 kPa MTHF. Trend lines (---) reflect exponential fits.

Figure S16 displays the formation rate of pentane (r_{pentane}) as a function of [MTHF], [H₂], [CO], [NH₃] and inverse temperature. Pentane formation rates follows similar trends to the reported C-O bond rupture rates over 12 nm Ni₂P that demonstrated a decrease in dependence of [MTHF] with increasing [MTHF] (Figure 3), weak inverse dependence in [CO] (Figure 4), and inverse first order dependence in [NH₃] (Figure 10); however, pentane formation rates show a much weaker inverse dependence in [H₂] ($r_{\text{pentane}} \sim [\text{H}_2]^{-0.16}$) than either C-O bond rupture pathway ($r_{2\text{C-O}} \sim [\text{H}_2]^{-1}$ and $r_{3\text{C-O}} \sim [\text{H}_2]^{-1/2}$ at $[\text{H}_2] < 1$ MPa and $r_{2\text{C-O}} \sim [\text{H}_2]^{-3/2}$ and $r_{3\text{C-O}} \sim [\text{H}_2]^{-1}$ at $[\text{H}_2] > 1$ MPa). Moreover, the activation enthalpy (ΔH^\ddagger) for pentane formation is more than 100 kJ mol⁻¹ greater than for either C-O bond rupture at 1 MPa H₂ and below 543 K (Figure S18b and Table S4, 127 kJ mol⁻¹ for pentane formation compared to 23 and 18 kJ mol⁻¹ for ²C-O and ³C-O bond rupture, respectively). The significant difference of r_{pentane} dependence on [H₂] and ΔH^\ddagger compared with $r_{2\text{C-O}}$ and $r_{3\text{C-O}}$ combined with the coexistence of high selectivity towards pentane (Figure S1) and presence of Brønsted acid sites on 12 nm Ni₂P strongly suggests that a separate C-O bond rupture pathway occurs over the Brønsted acid sites to form significant amounts of pentane, while the other C-O bond rupture products (e.g., 2-pentanone, 2-pentanol, butane) form over the Ni₂P surface.

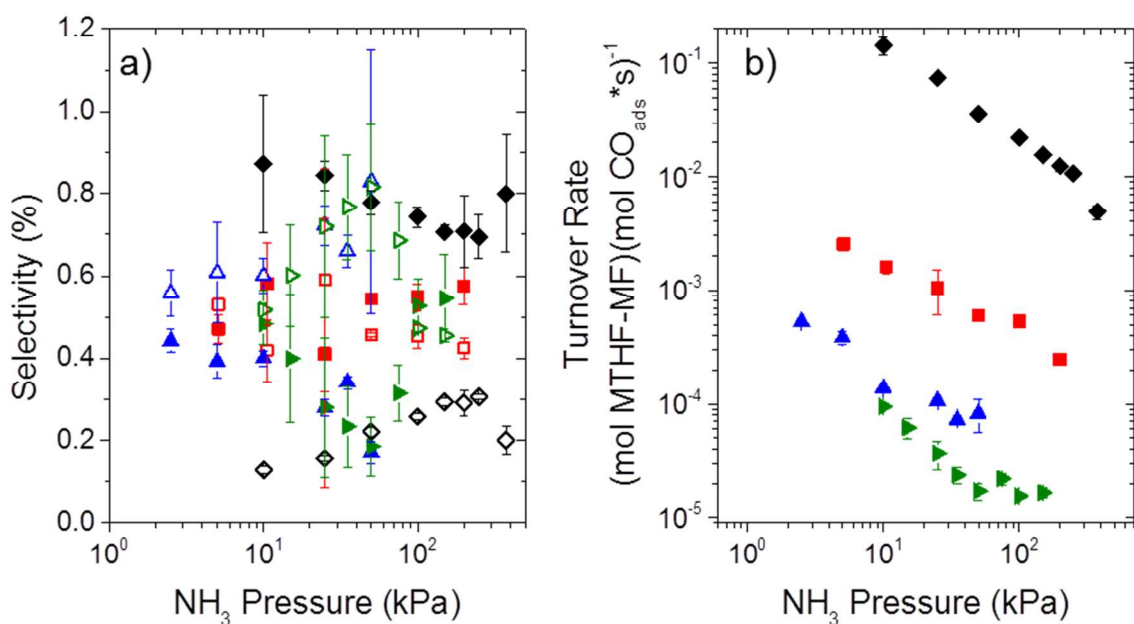


Figure S17. Changes in selectivity (a) for formation of pentanal and subsequent $^3\text{C-O}$ bond rupture products (hollow), and 2-penten-4-one and subsequent $^2\text{C-O}$ bond rupture products (filled) indicated in Scheme 1 and changes in the rate of consumption of the MTHF-MF reactant pool towards $^m\text{C-O}$ bond rupture products (b) with NH_3 pressure over SiO_2 supported 4 nm Ni (\blacklozenge), 5 nm Ni_{12}P_5 (\blacktriangleright), 19 nm Ni_{12}P_5 (\blacklozenge), and 12 nm Ni_2P (\blacktriangle) in 0.25 MPa H_2 and 5 kPa MTHF at 543 K.

S2. Derived expressions for rates CO-, H-, and C₅H₁₀O-covered surfaces using Transition State Theory

For a CO*-covered surface:

$$\text{C}_5\text{H}_{10}\text{O} + \text{CO}^* \xrightleftharpoons{K_{m_{C-O}}^\ddagger} \left(2 - \frac{m}{2}\right) \text{H}_2 + {}^m\text{C}_5\text{H}_{6+m}\text{O}^* \ddagger + \text{CO}$$

$$\frac{r_{m_{C-O}}}{[L]} = \frac{k_b T}{h} K_{m_{C-O}}^\ddagger \frac{[\text{MTHF}][\text{H}_2]^{-\frac{4-m}{2}}}{[\text{CO}]}$$

$$\frac{r_{m_{C-O}}}{[L]} = \frac{k_b T}{h} e^{\Delta S^\ddagger/R} e^{-\Delta H^\ddagger/RT} \frac{[\text{MTHF}][\text{H}_2]^{-\frac{4-m}{2}}}{[\text{CO}]}$$

For a H*-covered surface:

$$\text{C}_5\text{H}_{10}\text{O} + \text{H}^* \xrightleftharpoons{K_{m_{C-O}}^\ddagger} \left(\frac{5}{2} - \frac{m}{2}\right) \text{H}_2 + {}^m\text{C}_5\text{H}_{6+m}\text{O}^* \ddagger$$

$$\frac{r_{m_{C-O}}}{[L]} = \frac{k_b T}{h} K_{m_{C-O}}^\ddagger [\text{MTHF}][\text{H}_2]^{-\frac{5-m}{2}}$$

$$\frac{r_{m_{C-O}}}{[L]} = \frac{k_b T}{h} e^{\Delta S^\ddagger/R} e^{-\Delta H^\ddagger/RT} [\text{MTHF}][\text{H}_2]^{-\frac{5-m}{2}}$$

For a C₅H₁₀O*-covered surface:

$$\text{C}_5\text{H}_{10}\text{O}^* \xrightleftharpoons{K_{m_{C-O}}^\ddagger} \left(\frac{4-m}{2}\right) \text{H}_2 + {}^m\text{C}_5\text{H}_{6+m}\text{O}^* \ddagger$$

$$\frac{r_{m_{C-O}}}{[L]} = \frac{k_b T}{h} K_{m_{C-O}}^\ddagger [\text{H}_2]^{-\frac{4-m}{2}}$$

$$\frac{r_{m_{C-O}}}{[L]} = \frac{k_b T}{h} e^{\Delta S^\ddagger/R} e^{-\Delta H^\ddagger/RT} [\text{H}_2]^{-\frac{4-m}{2}}$$

Here m is the coordination of the C-atom to non-H atoms involved in the ^mC-O bond rupture within MTHF.

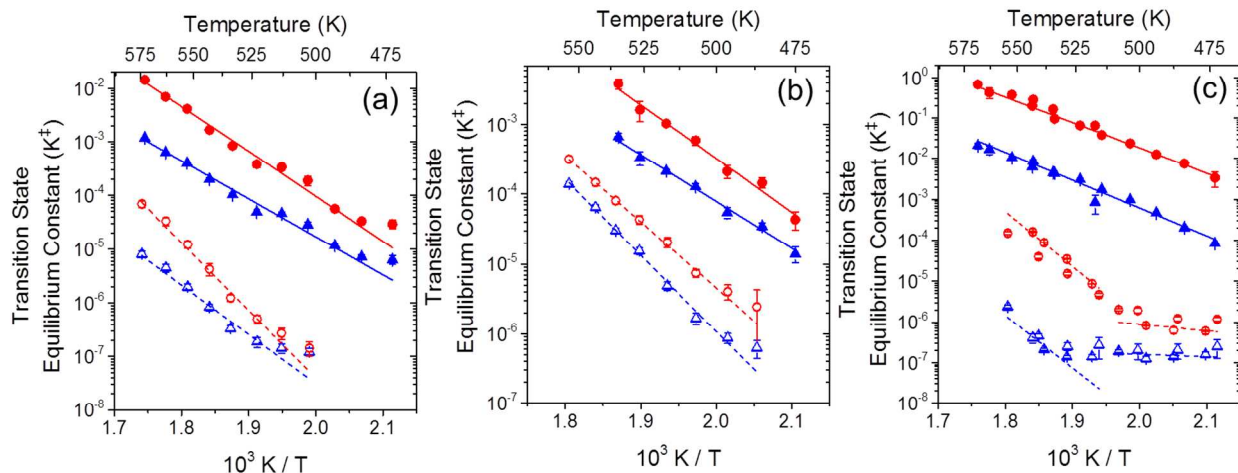


Figure S18. Changes in transition state equilibrium constant (K^\ddagger) as a function of inverse temperature of silica supported (a) 19 nm Ni_{12}P_5 , (b) 5 nm Ni_{12}P_5 , and (c) 4 nm Ni for $^2\text{C-O}$ (\bullet) and $^3\text{C-O}$ (\blacktriangle) bond rupture pathways in 5 kPa MTHF (filled, 1 MPa H_2 ; open, 1 MPa H_2 with 5 kPa CO). Trend lines are exponential fits weighted by the error bars. Full description of error analysis detailed in Section S5.

Table S4. Measured activation enthalpies (kJ mol^{-1}) for $^2\text{C-O}$ and $^3\text{C-O}$ bond rupture pathways over SiO_2 -supported catalysts beginning from $\text{C}_5\text{H}_{10}\text{O}^*$ -, H^* -, and CO^* -covered surfaces in 5 kPa MTHF extracted from Figures 11 and S18.

Catalyst	$\text{C}_5\text{H}_{10}\text{O}^*$		H^*		CO^*	
	$^2\text{C-O}$	$^3\text{C-O}$	$^2\text{C-O}$	$^3\text{C-O}$	$^2\text{C-O}$	$^3\text{C-O}$
12 nm Ni_2P	193±9	170±9	23±34	18±9		
19 nm Ni_{12}P_5	180±5	155±5			250±11	197±10
5 nm Ni_{12}P_5	144±12	134±12			183±3	215±6
4 nm Ni	119±8	130±4	30±17	12±13	255±16	248±72

Table S5. Difference in measured activation enthalpies (kJ mol^{-1}) for $^2\text{C-O}$ and $^3\text{C-O}$ bond rupture pathways over SiO_2 -supported catalysts between $\text{C}_5\text{H}_{10}\text{O}$ -covered and H^* -covered surfaces, and CO^* -covered and $\text{C}_5\text{H}_{10}\text{O}^*$ -covered surfaces in 5 kPa MTHF derived from values displayed in Table S4.

Catalyst	$\text{C}_5\text{H}_{10}\text{O}^*-\text{H}^*$		$\text{CO}^*-\text{C}_5\text{H}_{10}\text{O}^*$	
	$^2\text{C-O}$	$^3\text{C-O}$	$^2\text{C-O}$	$^3\text{C-O}$
12 nm Ni_2P	170±35	152±12	-	-
19 nm Ni_{12}P_5	-	-	69±12	42±11
5 nm Ni_{12}P_5	-	-	39±12	81±13
4 nm Ni	89±18	118±14	135±18	117±72

S3. Materials, Methods, and Characterization

S3.1. Synthesis and Characterization of Supported Nickel and Nickel Phosphide Catalysts

S3.1.1. Synthesis of Silica Supported Nickel and Nickel Phosphide Clusters

High surface area silica (SiO_2 , Sigma-Aldrich, Davisil Grade 646, 35-60 mesh, pore volume $1.15 \text{ cm}^3 \text{ g}^{-1}$) was washed with deionized (DI) water and dried in stagnant air at 353 K for over 10 h. Nickel phosphide catalysts were prepared using strong electrostatic adsorption (SEA)¹ or incipient wetness impregnation (IWI) methods. The SEA method involved adding the nickel precursor ($\text{Ni}(\text{NO}_3)_2 \cdot (\text{H}_2\text{O})_6$, 0.428 g, Sigma Aldrich, $\geq 97.0\%$) to 265 cm^3 of DI water (Barnstead E-Pure, 17.6 M Ω) and mixed until completely dissolved. An NH_4OH aqueous solution (20 cm^3 , Macron, 28-30% NH_3) was added to the precursor solution, to form an aqueous $[\text{Ni}(\text{NH}_3)_6]^{2+}$ complex.¹ Then 4.424 g of SiO_2 were added to 285 cm^3 of the aqueous solution and stirred for 4 h at 298 K. The solids were then separated from the liquid by vacuum filtration and rinsed with 2 L DI water. Samples were prepared by IWI by creating an aqueous solution of the same nickel precursor and adding 5.75 cm^3 of this solution dropwise to 5 g of clean, dry SiO_2 achieving incipient wetness. Wet solids derived from both SEA and IWI were dried in stagnant air for 48 h at 333 K. Subsequently, the dried solids were heated to 773 K at 0.05 K s^{-1} and held at 773 K for 5 h in flowing dry air ($8.3 \text{ cm}^3 \text{ s}^{-1}$, S.J. Smith, Ultra Zero). Samples were then cooled to 323 K in He (S.J. Smith, 99.99%) and then heated to 963 K at 0.05 K s^{-1} and held for 2 h in flowing 10% H_2/He ($8.3 \text{ cm}^3 \text{ s}^{-1}$, S.J. Smith, 99.999%) with the intent to reduce the Ni to a metallic state. Lastly, samples were cooled to ambient temperature in He and then passivated in flowing mixture of 20% dry air and 80% He ($8.3 \text{ cm}^3 \text{ s}^{-1}$) for 3 h.

A sample of the Ni- SiO_2 was set aside (1.9 wt. %) while the remaining Ni- SiO_2 was impregnated with 0.14 M phosphorous acid solution (Sigma Aldrich, H_3PO_3 solution $\geq 50\%$) in 0.1 cm^3 aliquots to achieve a molar Ni:P ratios of 2:1 or 1:1 for Ni_{12}P_5 and Ni_2P catalysts, respectively. These samples were dried for 48 h at 333 K in ambient air and then heated to 773 K at 0.05 K s^{-1} and held for 5 h to dry air ($8.3 \text{ cm}^3 \text{ s}^{-1}$, S.J. Smith, Ultra Zero). Samples were then cooled to 323 K in He (S.J. Smith, 99.99%) followed by a reductive treatment in 10% H_2 and 90% He ($8.3 \text{ cm}^3 \text{ s}^{-1}$, S.J. Smith, 99.999%) heated to 963 K at 0.05 K s^{-1} and held for 2 h with the intent to reduce the phosphorus and form a nickel phosphide ceramic. The reduced samples were cooled to ambient temperature in He and passivated in in flowing mixture of 20% dry air and 80% He ($8.3 \text{ cm}^3 \text{ s}^{-1}$) for 3 h.

S3.1.2. Powder X-ray Diffraction

The crystallographic structures of $\text{Ni}_{12}\text{P}_5\text{-SiO}_2$ and $\text{Ni}_2\text{P-SiO}_2$ materials were determined using powder x-ray diffraction (XRD) measured using a Siemens/Bruker D-5000 (Cu K- α , 0.15418 nm). High weight loading catalysts (18 wt. %) were used to have obtain observable diffraction patterns. Approximately 300 mg of each sample was finely ground using mortar and pestle and scanned at a rate of $0.0167^\circ \text{ s}^{-1}$ with 0.1° resolution. Ni_{12}P_5 and Ni_2P nanoparticles used for spectroscopic and kinetic measurements were prepared similarly but scanned at a rate of $0.00167^\circ \text{ s}^{-1}$ with 0.02° resolution. Figure S15 shows the diffraction patterns of the materials after applying a Fourier transform smoothing filter with a fifteen-point window. Lower weight loading materials do not shown strong crystallographic features with the exception of 19 nm Ni_{12}P_5 . The diffraction patterns from the high weight loading materials and 19 nm Ni_{12}P_5 closely agree with published results for Ni_{12}P_5 and Ni_2P powders.²

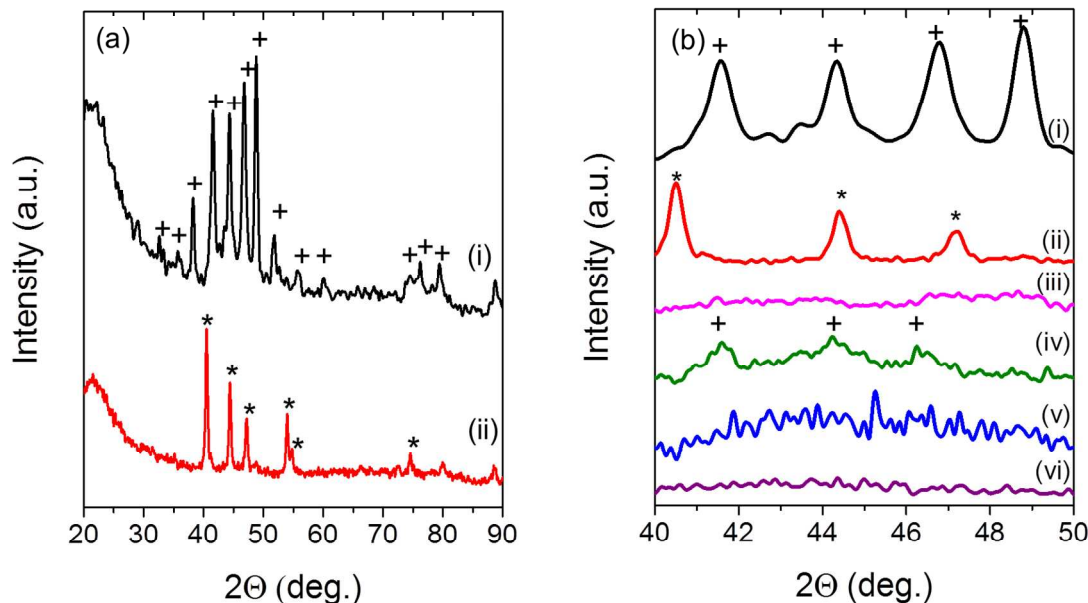


Figure S19. Diffractograms of SiO₂ supported Ni₁₂P₅ and Ni₂P nanoparticles at high weight loadings (18 wt% Ni) synthesized with Ni:P molar ratios of 2:1 (i, black) and 1:1 (ii, red), and diffractograms of low weight loading Ni₁₂P₅ and Ni₂P nanoparticles used for kinetic and spectroscopic measurements 12 nm Ni₂P (iii, pink), 19 nm Ni₁₂P₅ (iv, green), 5 nm Ni₁₂P₅ (v, blue), and 10 nm Ni₁₂P₅ (vi, purple). Assignments for crystallographic features (Ni₁₂P₅ (+) and Ni₂P (*)) are based on previous reports.² Excess P is known to leave as PH₃ during synthesis.³

S3.1.3. Metal Phosphide Cluster Sizes and Composition

Cluster diameters were measured using transmission electron microscopy (TEM) on a JEOL 2010-LaB₆ (200 kV) equipped with a digital camera (Gatan MatScan 1k × 1k progressive scan CCD). TEM samples were prepared by grinding approximately 10 mg of sample to a fine powder and dusting onto a 200 mesh holey carbon copper grid (Ted Pella Inc.). The diameters of more than 300 particles were counted from the TEM images obtained to calculate surface area normalized average cluster diameters ($\langle d_{TEM} \rangle$, Table 2) for each sample using the following equation:

$$\langle d_{TEM} \rangle = \frac{\sum_i n_i d_i^3}{\sum_i n_i d_i^2} \quad (\text{S3})$$

where n_i is the number of cluster with diameter, d_i . Sample images and cluster size distributions for each catalyst are shown Figures S20-S24.

Chemisorbed CO was used to measure the number of exposed surface sites per mole of Ni atoms assuming a Ni ensemble site. Approximately 100 mg of sample was added to a U-shaped Pyrex reactor in a packed bed configuration. After pumping down the manifold and cell using vacuum pumps (Edwards EXT250 backed by Varian SH-100) for 12 h, the sample was treated in H₂ to 673 K at 0.05 K s⁻¹ (direct read rotameter, Omega, FLD series) and held for 1 h. The H₂ flow was stopped and the system was held under vacuum for 1 h at 673 K and then cooled to 303 K under vacuum. Prior to taking measurements, the cell was isolated from the manifold to fill the manifold with an initial pressure of CO (Praxair, 99.99%). The gas was then expanded into the cell and the equilibrated pressure was recorded using one of two Baraton capacitance manometers (MKS, 10 Torr, 1000 Torr). Total uptake of CO for all materials are shown in Table 2, and adsorption isotherms for each sample are shown in Figure S25.

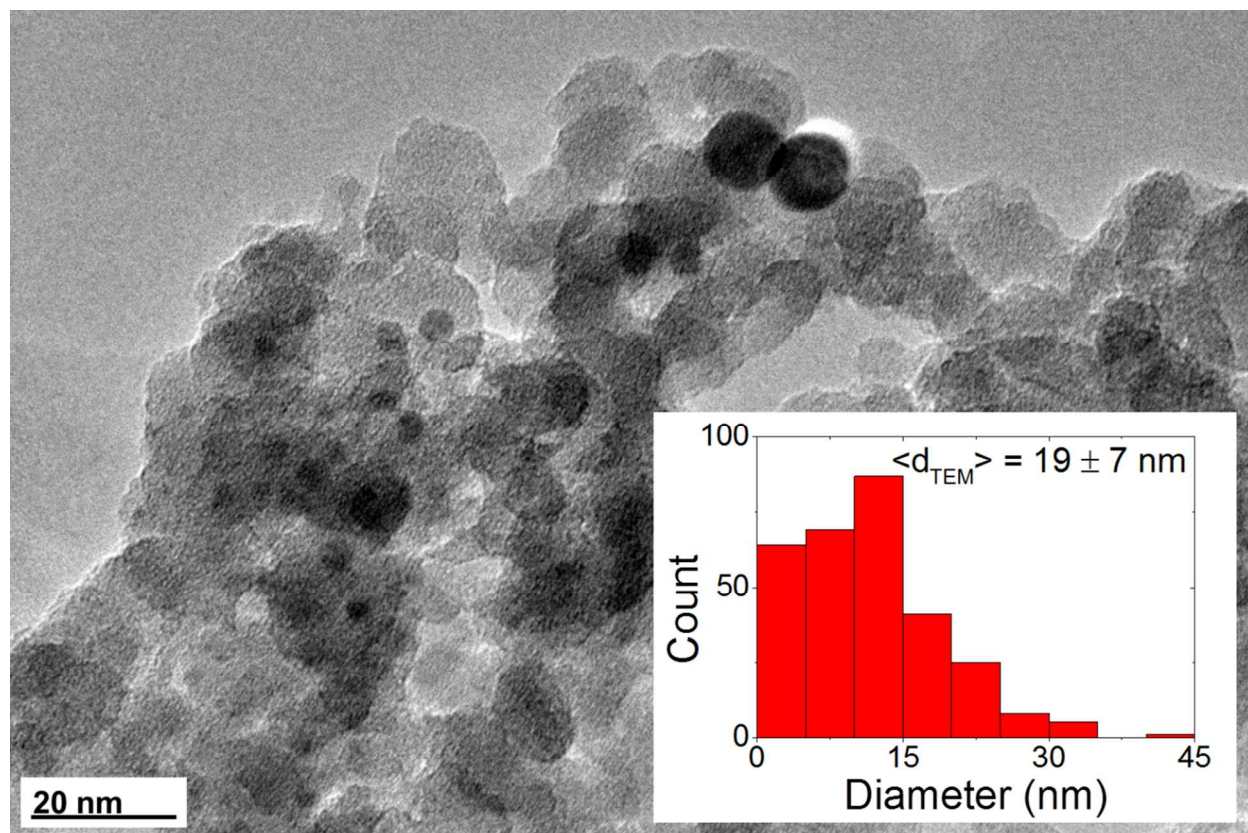


Figure S20. TEM image of Ni_{12}P_5 on silica support with surface area normalized. Average cluster size of $19 \pm 7 \text{ nm}$.

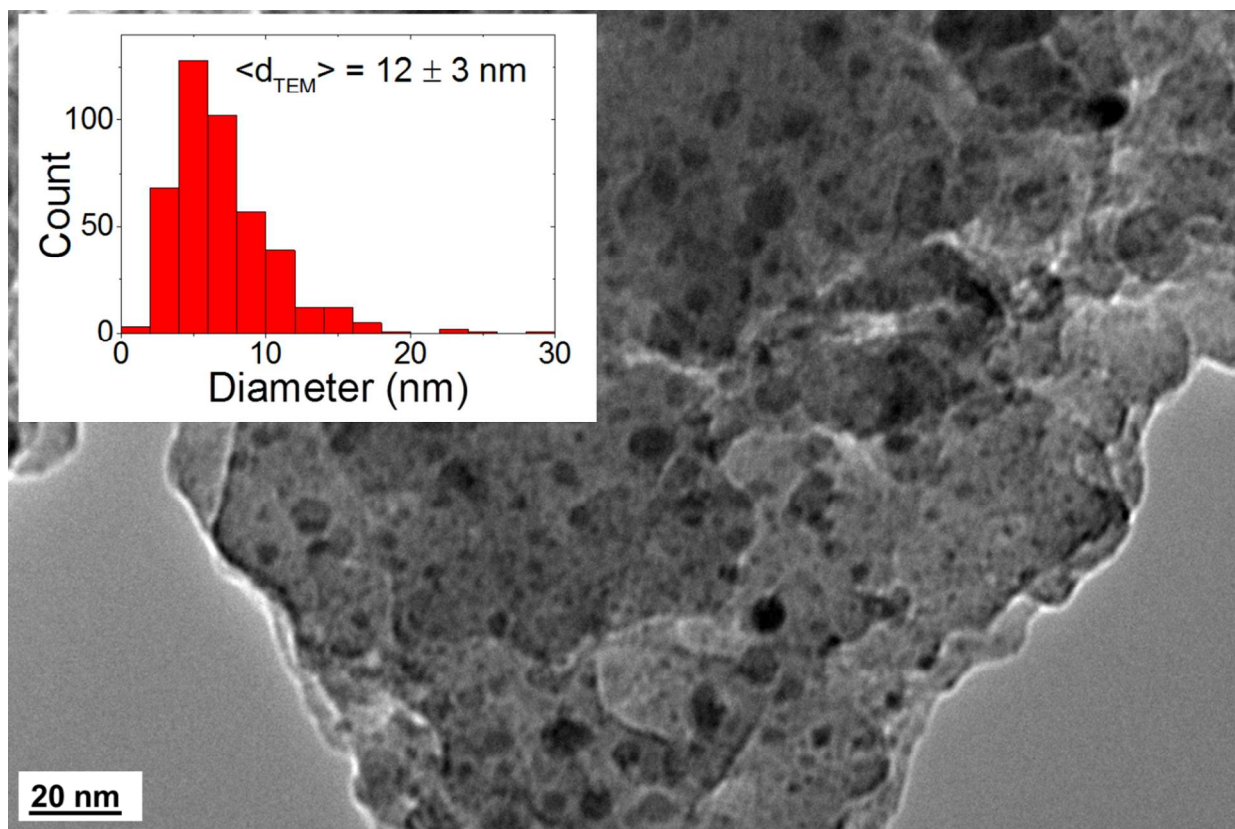


Figure S21. TEM image of Ni₂P on silica support with surface area normalized. Average cluster size of 12±3 nm.

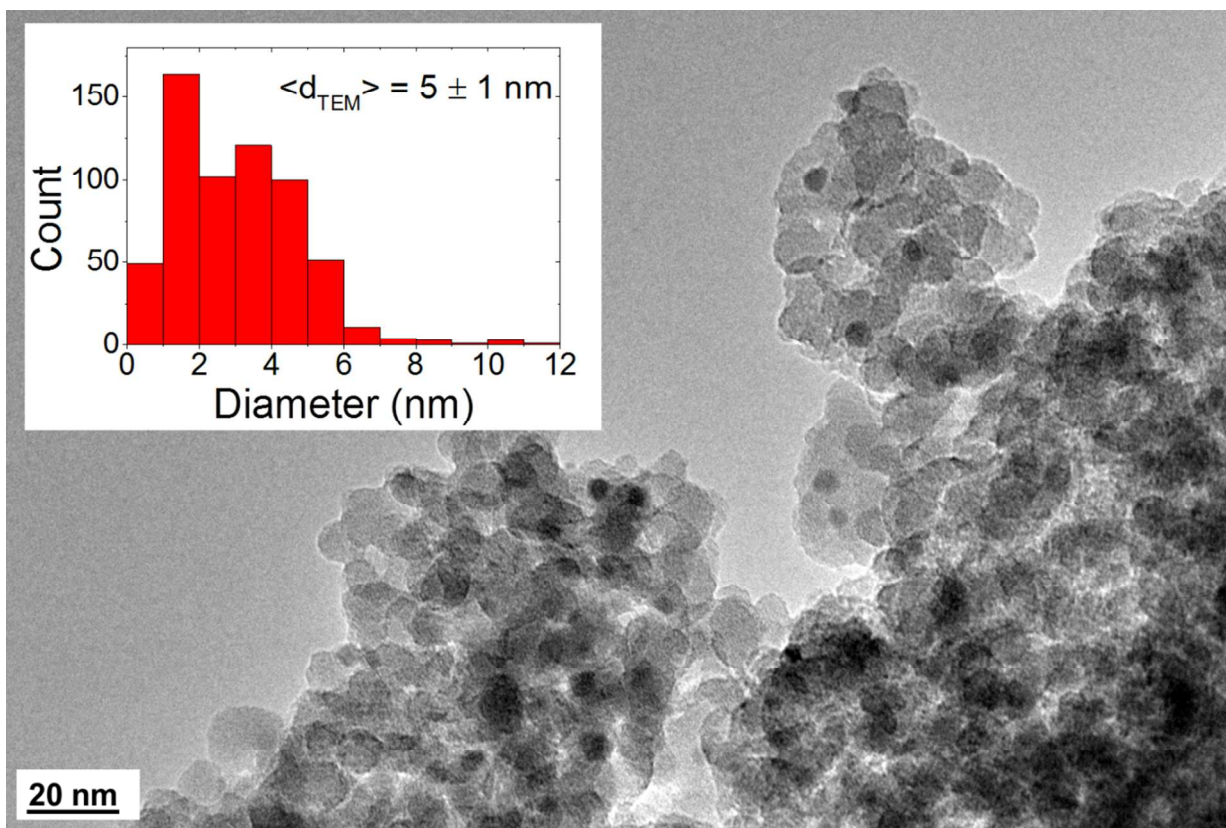


Figure S22. TEM image of Ni₁₂P₅ on silica support with surface area normalized. Average cluster size of 5±1 nm.

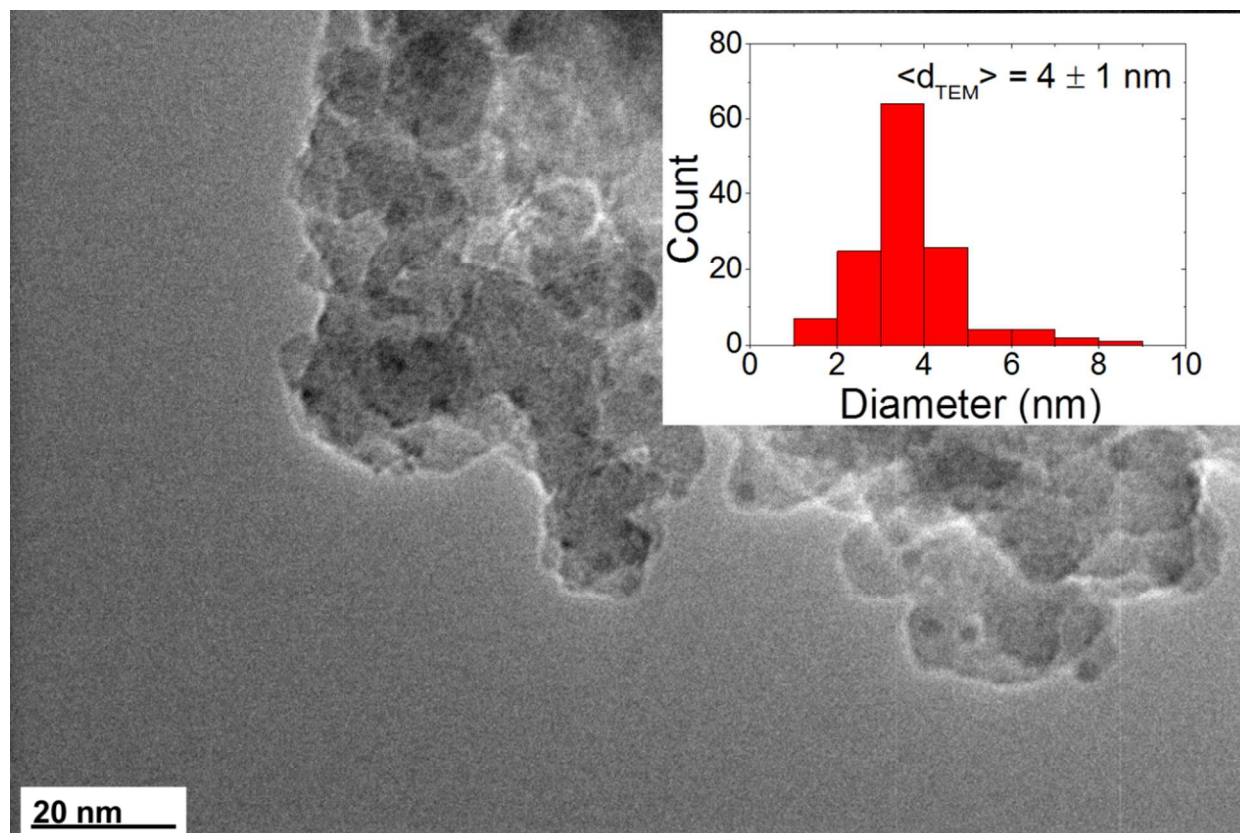


Figure S23. TEM image of Ni on silica support with surface area normalized. Average cluster size of 4 ± 1 nm.

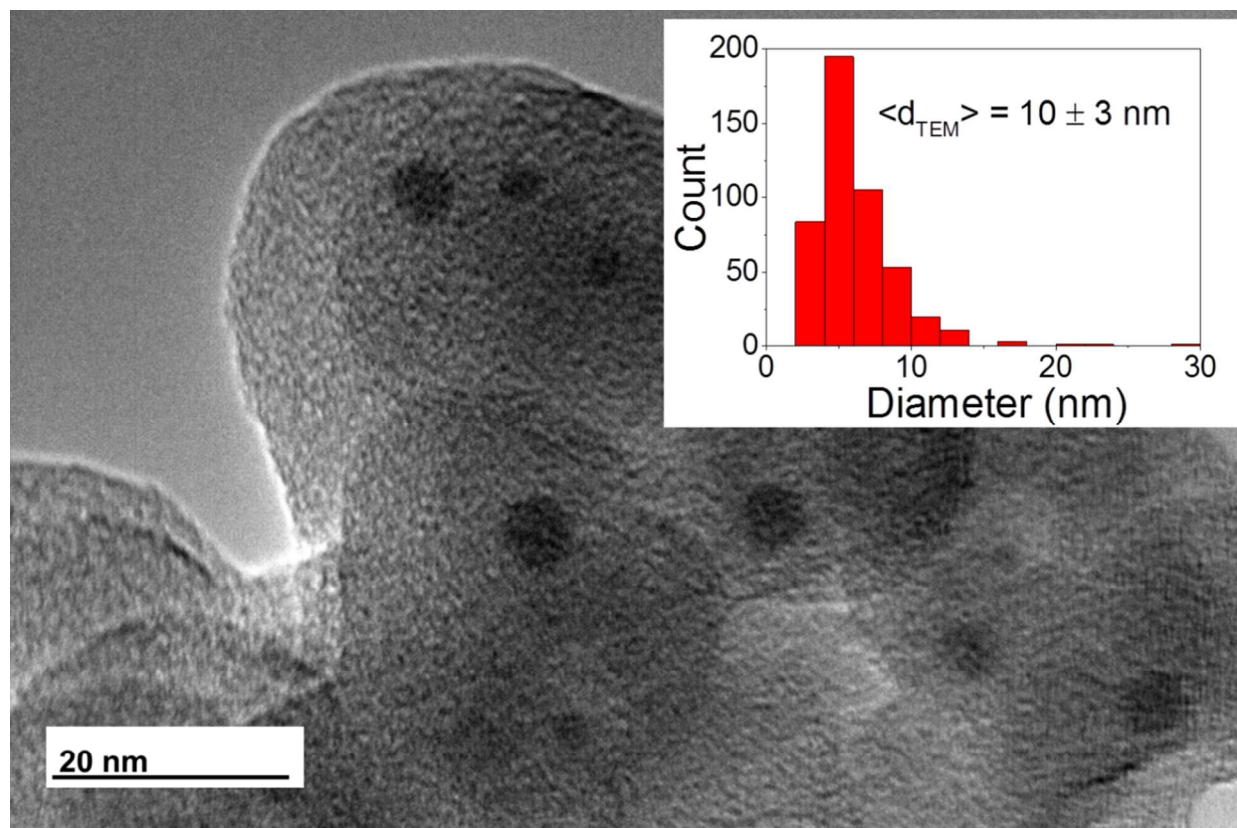


Figure S24. TEM image of Ni_{12}P_5 on silica support with surface area normalized. Average cluster size of $10 \pm 3 \text{ nm}$.

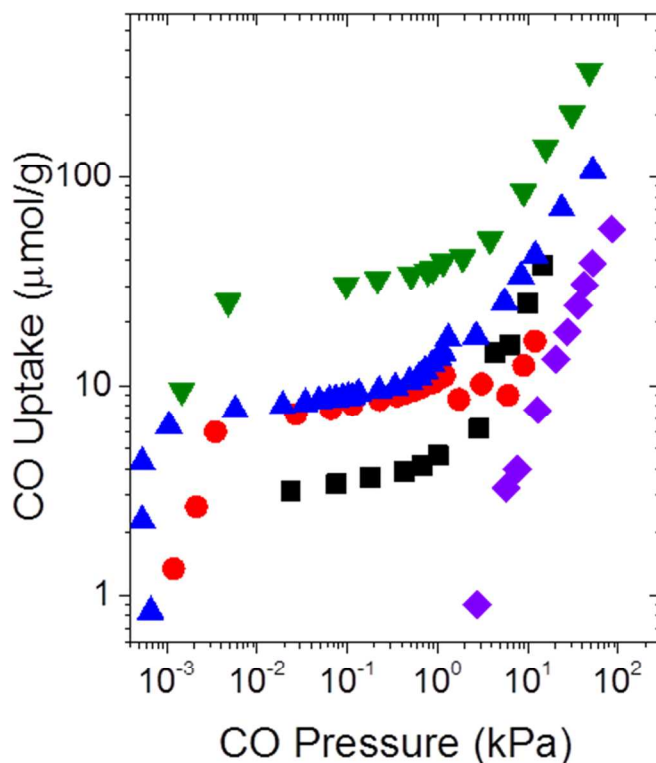


Figure S25. Adsorption isotherms at 298 K for CO on silica supported 19 nm Ni_{12}P_5 (■), 5 nm Ni_{12}P_5 (▼), 12 nm Ni_2P (●), and 4 nm Ni (▲), and dried SiO_2 (◆). Uptake normalized by mass of catalyst material.

CO uptake is used to normalize turnover rates for catalysts. Silica shows uptake of CO at CO pressures greater than 2 kPa and significant uptake at pressures greater than 10 kPa, which is seen in the adsorption isotherms of all silica supported catalysts after the uptake has appeared to plateau. To avoid including contributions of silica in the normalization of turnover rates over Ni, Ni_{12}P_5 , and Ni_2P nanoparticles, CO uptake values were determined at ~1 kPa CO.

S3.1.4. Temperature Programmed Reduction of Catalysts

Temperature programmed reduction (TPR) was performed on dried Ni, Ni_{12}P_5 , and Ni_2P samples in order to confirm that the Ni, Ni_{12}P_5 , and Ni_2P materials were reduced by the thermal treatments in H_2/He mixtures. The samples (~100 mg) were supported on a quartz frit fused within a quartz tubular reactor (9.8 mm inner diameter), which was held within an electrically heated furnace (Lindberg Hevi-Duty) controlled by an electronic temperature controller (Watlow, EZ-Zone). The temperature of the sample was monitored by a K-type thermocouple (Omega) inserted into a glass nipple that protruded into the catalyst bed. Gas flow rates were controlled using mass flow controllers (Parker Porter, Model 601) with a digital controller (Parker Porter, CM-400). The composition of the effluent gas was monitored using a quadrupole mass spectrometer (QMS) (Pfeiffer Vacuum, ThermoStar).

Prior to TPR experiments, the samples were heated to 773 K at 0.05 K s^{-1} and held for 6 h in flowing dry air (100 ml min^{-1} , purified using a zero air generator (Parker, 76-830)) with the intent to fully oxidize the samples. Samples were then cooled to 303 K after which the system was flushed with 10% H_2 (S.J. Smith, 99.999%) / 90% He (S.J. Smith, 99.99%) for 1 h. The composition of the exiting gas stream became

stable after 1 h at which point the sample was heated to 1073 K at 0.05 K s^{-1} while the H_2 consumption and H_2O production were monitored as a function of sample temperature using the QMS. Figure S22 shows reduction profiles indicating the formation of a nickel phosphide phase as opposed to separate nickel and phosphide phases, because the Ni_{12}P_5 and Ni_2P reduction profiles are not a linear combination of the $\text{Ni}(\text{NO}_3)_2$ and H_3PO_3 reduction profiles, rather the presence of Ni decreases the reduction temperature of the phosphite group.

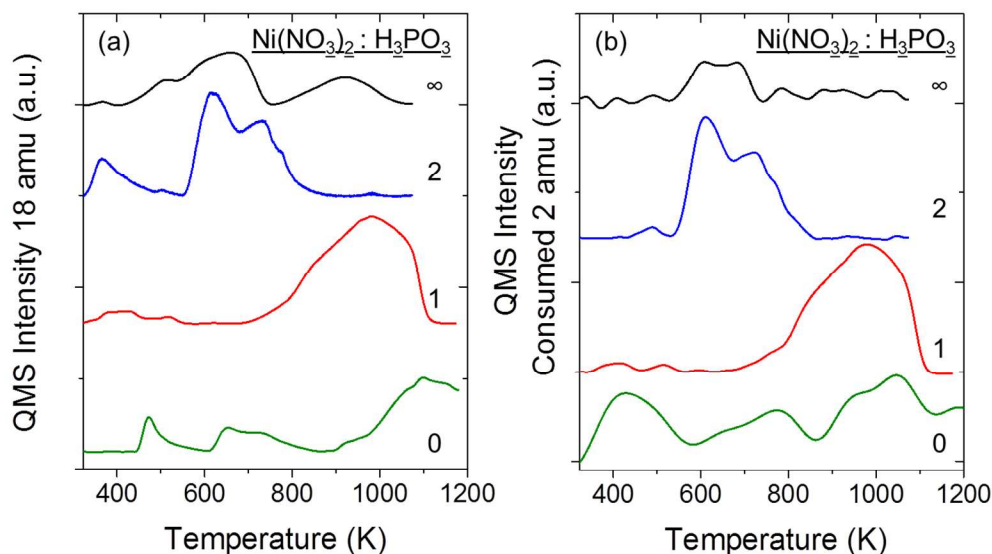


Figure S26. Measured intensity for 18 amu (a) and 2 amu (b) normalized by 4 amu during temperature programmed reduction of $\text{Ni}(\text{NiO}_3)_2$ on SiO_2 , H_3PO_3 on Ni-SiO_2 at $\text{Ni}(\text{NO}_3)_2 : \text{H}_3\text{PO}_3$ ratios of 1 and 2, and H_3PO_3 on SiO_2 in $50 \text{ cm}^3 \text{ min}^{-1}$ of 10% H_2 and 90% He at 3 K min^{-1} following an oxidative treatment in $50 \text{ cm}^3 \text{ min}^{-1}$ dry air at 773 K for 6 h.

Raw intensities were normalized by the measured intensity of 4 amu (i.e., He) to account for any drift in the internal pressure of the mass spectrometer and the baselines were corrected using the spline function in Origin Pro. Intensities were inverted for 2 amu as H_2 is consumed during the reductive treatment.

S3.1.5. *In Situ* Fourier Transform Infrared Spectroscopy

Reactive intermediates and basic probe molecules (i.e., pyridine) formed or adsorbed during hydrogenolysis of 2-methyltetrahydrofuran (MTHF) over Ni, Ni_{12}P_5 , and Ni_2P catalysts were observed using *in situ* transmission Fourier transform infrared (FTIR) spectroscopy using a custom-made transmission cell, previously described,⁴ with a spectrometer (Bruker, TENSOR 37) equipped with a liquid- N_2 cooled HgCdTe detector. Self-supporting catalyst pellets ($25 \pm 5 \text{ mg}$) were made by grinding SiO_2 -supported Ni, Ni_{12}P_5 , and Ni_2P catalysts to a fine powder in a ceramic mortar and pestle and pressing the catalyst in a stainless steel template (20.43 mm diameter) using a manual bench-top press (Carver Laboratory Press). The formed catalyst pellets were placed within the stainless-steel transmission cell equipped with CaF_2 windows and connected to a gas manifold. Liquid reactants (MTHF, Sigma Aldrich, $\geq 99.5\%$; and pyridine, Fisher, $\geq 99.9\%$) were introduced through a septum 35 cm upstream of the catalyst using a syringe pump (KD Scientific, Legato 100) in a crossflow configuration with the primary gas flow (H_2 , S.J. Smith, 99.999%; and He, S.J. Smith, 99.99%) controlled by mass flow controllers (Alicat). Transfer lines were heated to 523 K with heating tape (Omega, FGH series) to vaporize liquid reactants. The transmission cell was heated using resistive heating cartridges controlled with an electronic PID controller (Watlow, EZ-Zone), and the temperature was measured with a K-type

thermocouple adjacent to the self-supporting catalyst pellet. Prior to acquiring spectra, the catalyst was pretreated *in situ* to 673 K at a rate of 0.05 K s⁻¹ and held for 1 h in 20 cm³ min⁻¹ H₂ at ambient pressure. The cell was then allowed to cool to 543 K while remaining under H₂ flow. The background IR spectra were collected under a flow of 15 kPa He and 86 kPa H₂ at 543 K following the *in situ* pretreatment. Steady state measurements were obtained while flowing 5 kPa MTHF, 80 kPa H₂, and 16 kPa He prior introducing 1 kPa pyridine (while reducing the He pressure to 15 kPa to maintain constant total pressure). Spectra were collected at a resolution of 4 cm⁻¹ and averaged over 128 scans for both the initial background and measured steady-state conditions. All spectra acquisition was performed using Bruker Corporation's OPUS Spectroscopy Software 7.0.129.

The subsequent spectra analysis (e.g., subtraction of gas phase contribution, baseline correction, and data smoothing) was performed using OriginLab's OriginPro software. Spectra obtained from *in situ* experiments were baselined corrected using Origin Pro using the peak analyzer tool with 8 -12 anchor points and interpolating with the spline function. Spectra were obtained over an 80 mg SiO₂ pellet at 543 K and 5 kPa MTHF. These spectra were normalized to be representative of the same pellet thickness (25 mg) as the silica supported Ni, Ni₁₂P₅, and Ni₂P pellets. Contributions from gas phase MTHF and MTHF adsorbed to SiO₂ were removed by subtracting spectra obtained over a SiO₂ pellet; therefore, remaining spectral features are representative of adsorbates on the Ni, Ni₁₂P₅, and Ni₂P surfaces.

Preparation of the IR pellet requires first weighing 25 mg (\pm 5 mg) of the dry catalyst. The catalyst is then ground into a fine powder ($>$ 200 mesh) using a ceramic mortar and pestle. The pellet mold is comprised of two 20.34 mm diameter stainless steel cylinders (heights of 32.42 mm and 15.97 mm) and a rectangular stainless steel casting (63.5 mm x 38.18 mm x 50.05 mm) with a 20.39 mm cylindrical orifice centered on the shortest side to serve as the structural support for the die body and plunger. The longer of the two cylinders is placed into the support structure and the ground catalyst is poured into the center of the mold. The top piston is then placed on top of the ground catalyst and rotated in a circular motion to ensure an even distribution of the catalyst powder. This assembly was then placed in a Fred S. Carver Inc. Carver Laboratory Press and a pressure of 5000 psig was applied to the assembly for 60 seconds. The applied force was then increased to 10,000 psig for an additional 60 seconds. The assembly was then removed from the press and the casting was lifted from the cylindrical pistons and the resulting IR pellet was loaded into the primary cell.

S3.2. Catalytic Rate Measurements

S3.2.1. Reactor Design and Operation

Rate and selectivity measurements were conducted in a packed bed reactor comprised of stainless steel tube (3/8" OD) containing ~10-500 mg of catalyst, which was held at the center of the reactor using glass rods and packed glass wool. The reactor was heated with a three-zone electrically heated furnace (Applied Test Systems, 3210) that was controlled by an electronic temperature controller (Watlow, EZ-Zone). The catalyst temperature was measured by a K-type thermocouple contained within a 1/16" stainless steel sheath (Omega) that was coaxially aligned within the reactor and submerged within the catalyst bed. The volume of the catalyst bed was kept constant at 1.4 cm³ of material by mixing excess SiO₂ (dried at 353 K in ambient air) with the desired mass of catalyst. The system was pressurized (0.1-6.0 MPa) using a dome loaded back pressure regulator (BPR, Mitey Mite, S91XW), which was controlled by an electronic pressure regulator (EPR, Proportion-Air, BB1). The reactor pressure was monitored upstream and downstream of the catalyst bed using a digital pressure gauge (Omega, DPG-1000L) and the EPR, respectively. Comparisons of these measurements showed that the pressure drop across the catalyst bed was less than 1% of the total pressure.

Gas flow rates (H₂, CO (S.J. Smith, 1.03% CO, balance H₂), and NH₃ (S.J. Smith, \geq 99.999%)) were controlled using mass flow controllers (Parker Porter, Model 601) coupled to a digital controller (Parker Porter, CM-400). The flow rates of liquids including 2-methyltetrahydrofuran (MTHF, Sigma Aldrich, \geq 99.5%) and 2-methylfuran (MF, Aldrich Chemistry, 99%), were controlled using a stainless steel syringe

pump (Teledyne Isco, 500D with D-series controller) fed through a PEEK tube (1/16" outer diameter, 0.01" inner diameter) the exit of which was positioned within a small bed of non-porous sand (2.5 g, Sigma Aldrich, 50-70 mesh) within a cross flow of H₂. The transfer lines surrounding the liquid inlet were kept at 298 K for low pressures (< 8 kPa) of MTHF and heated to 393 K using heating tape (Omega, FGH series) for high pressures (> 10 kPa) of MTHF to avoid condensation. All transfer lines downstream of the liquid inlet were heated above 373 K at low MTHF pressures and 393 K at high MTHF pressures using heating tape to avoid condensation of the products or reactant. Line temperatures were monitored with K-type thermocouples (Omega) displayed on a digital reader (Omega, 402B-TC).

Catalysts were pretreated in situ by heating to 673 K at 0.05 K s⁻¹ and holding for 1 h within 101 kPa flowing H₂ (S.J. Smith, 99.999%) at 50 ml min⁻¹ prior to all catalytic measurements. The effluent of the reactor was characterized using on-line gas chromatography (Agilent, HP 6890). The gas chromatograph (GC) was equipped with a capillary column (HP Plot Q, 30 m length, 0.320 mm inner diameter, 20 μm) connected to a flame ionization detector to quantify the concentrations of combustible species and a packed column (HayeSep Q, 2 m length, 2 mm inner diameter) connected to a thermal conductivity detector to measure H₂, H₂O, CO, and CO₂. Sensitivity factors and retention times for all components were determined using gaseous and liquid standards. A complete list of these standards and calculations for sensitivity factors are shown in the Supporting Information (Section S3.2.2). Control of the reactor pressure and temperature, reactant flowrates, and the GC sampling were automated to allow for continuous measurements.

Conversions were calculated on a carbon basis based on the amount of carbon that appears in the products. The carbon and oxygen balance closes within ± 10%. Turnover rates are normalized by the number of CO adsorption sites determined through chemisorption experiments described in Section S3.1.3. Rate data over Ni clusters at [H₂] less than 1 MPa are not reported due to rapid deactivation that could not be corrected. Reactor conditions during rate and selectivity measurements were varied by sequentially decreasing and then increasing the reactant pressure over the full range such that one or more of the conditions is measured at least twice throughout the experiment to ensure that measured trends were not a result of systematic deactivation.

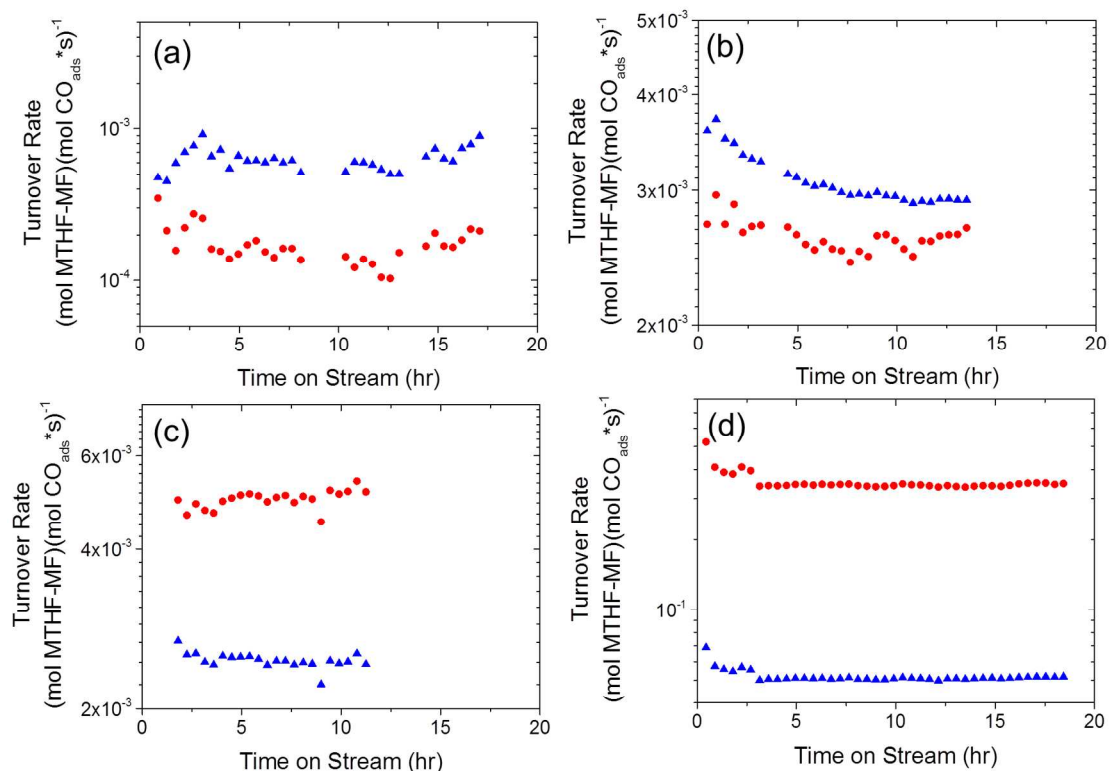


Figure S27. Measured rates of consumption of the MTHF-MF reactant pool to form pentanal and subsequent $^3\text{C-O}$ bond rupture products (\blacktriangle), and 2-penten-4-one and subsequent $^2\text{C-O}$ bond rupture products (\bullet) indicated in Scheme 1 as a function of time on stream over silica supported (a) 12 nm Ni_2P , (b) 5 nm Ni_{12}P_5 , (c) 19 nm Ni_{12}P_5 , (d) and 4 nm Ni at 5 kPa MTHF, 1 MPa H_2 , 543 K.

Catalysts underwent an initial break-in period in 5 kPa MTHF and 1 MPa H_2 at 543 K until the turnover rates and selectivity changed by less than 1% per hour before the reaction conditions were varied in kinetic experiments. Rates measured following the initial break in period were corrected for the number of active sites lost over time by fitting an exponential decay expression to the rates as a function of time:

$$r = r_0 \cdot e^{-\beta \cdot t} \quad (\text{S4})$$

$$\frac{[L]}{[L]_0} = \frac{r}{r_0} \quad (\text{S5})$$

Where t is the time on stream, r is the turnover rate at time t , r_0 is the initial turnover rate, β is the rate of decay, $[L]_0$ is the initial number of active sites and $[L]$ is the remaining number of active sites at time t . This benchmark condition (5 kPa MTHF, 1 MPa H_2 , 543 K) was regularly measured throughout a catalyst's time on stream to correct for any deactivation and ensure there was no systematic change in selectivity over time.

Water formed from dehydrating 1-pentanol and 2-pentanol does not appear to have any measurable inhibiting effects or lead to deactivation of the catalyst. While product inhibition is observed over all catalysts, as shown in Figure S4, the addition of co-fed CO eliminates the decrease in C-O bond rupture rates with increased conversion; thus, the product inhibition only appears to be caused by CO and not water. In combination with the regular measurements of the benchmark condition, no evidence indicates

that the amount of water produced under the conditions used within this study lead to deactivation of the Ni, Ni₁₂P₅, and Ni₂P nanoparticles.

S3.2.2 . Standards and Calibrated Sensitivity Factors for Gas Chromatograph

In all the experiments, 2-methyltetrahydrofuran (MTHF) was used as a standard to calibrate the pressures of the liquid reactants and products. Initially, a measured amount of MTHF was injected through the system by-pass and the gas chromatograph gas sampling valve. The sensitivity factor of MTHF, F_{MTHF} , was calculated by taking the ratio of the known pressure of the MTHF to the peak area as shown in the following equation,

$$F_{MTHF} = \frac{P_{MTHF}}{A_{MTHF}} \quad (S6)$$

where P_{MTHF} and A_{MTHF} are the pressure and measured peak area of MTHF, respectively. Sensitivity factors of other components were calculated by injecting known ratios of MTHF to other desired components directly to the capillary column of the GC. Since the mole ratio is proportional to the peak areas, the sensitivity factor of different components, F_i , were calculated using the following equation,

$$\frac{F_{MTHF} * A_{MTHF}}{F_i * A_i} = \frac{N_{MTHF}}{N_i} \quad (S7)$$

where A_i is the measured peak area and $\frac{N_{MTHF}}{N_i}$ is the mole ratio of MTHF to species i . Consequently, the pressures of the desired products were calculated utilizing the sensitivity factor derived above as shown in the following equation,

$$P_i = P_{MTHF} * F_i * \frac{A_i}{A_{MTHF}} \quad (S8)$$

Here, P_i is the pressure of species i in the effluent stream.

Gas species were calibrated by introducing a multi-component gas mixture into the GC through the gas sampling valve. Sensitivity factors were calculated by dividing the pressure by the peak area observed, using the equation

$$F_i = \frac{P_i}{A_i} \quad (S9)$$

The pressure of each species i (P_i) of the gases were calculated assuming the validity of the ideal gas law. Consequently, the pressures of the products were quantified by multiplying the sensitivity that was derived above by the peak area:

$$P_i = F_i * A_i \quad (S10)$$

The following chemicals were used as standards for the calibration of sensitivity factors and retention times:

- 2-methyltetrahydrofuran, Sigma-Aldrich, $\geq 99.5\%$
- 2-methylfuran, Aldrich Chemistry, 99%
- Tetrahydrofuran, Macron Fine Chemicals, ACS grade
- Diethyl ether, Fisher Scientific, 99.9%
- Methanol, OmniSolv, $\geq 99.9\%$

- Acetaldehyde, Fluka Analytical, $\geq 99.5\%$
- Ethanol, Decon Laboratory, 200 proof
- Furan, Aldrich, $\geq 99\%$
- Acetone, Macron Fine Chemicals, ACS grade
- Isopropanol Fisher Scientific, Certified grade
- Methyl-propyl-ether, Aldrich Chemistry, 97%
- 1-propanol, Fisher Scientific, Certified grade
- Valeraldehyde, Acros Organics, 97%
- 2-pentanone, Acros organics, $\geq 99\%$
- 2-pentanol, Aldrich Chemistry, 98%
- 1-pentanol Acros organics, 99%

The two separate multi-component gas mixtures were used to calibrate the gaseous species:

- Scotty Analyzed Gases, 15.5 ppm acetylene, 15.2 ppm n-butane, 15.2 ppm ethane, 15.1 ppm ethylene, 15.2 ppm methane, 15.1 ppm propane, 15.2 ppm propylene, 15.3 ppm methyl acetylene bal. nitrogen
- Scotty Analyzed Gases 1.01% acetylene, 1.0% carbon dioxide, 1.0% carbon monoxide, 1.01% ethane, 1.01% ethylene, 1.01% methane bal. nitrogen

Liquid mixtures were with MTHF to determine the relative peak area of each component to MTHF in comparison to the relative mol%.

Products without analytical standards were identified by comparing retention times of products with the same functional group plotting as a function of carbon number. Sensitivities were estimated in a similar fashion.

- 1-butene
- 2-butene
- 2-penten-4-one
- Penten-4-ol

S3.3. Computational Methods

S3.3.1. Nickel and Nickel Phosphide Lattice Parameters and Surface Formation Energies

Periodic plane-wave DFT calculations were performed using the Vienna *ab initio* simulation package (VASP).⁵⁻⁸ Plane waves were constructed using projector augmented-wave (PAW) potentials with an energy cutoff of 396 eV.^{9,10} The Perdew–Burke–Ernzerhof (PBE) form of the generalized gradient approximation (GGA) was used to determine exchange and correlation energies for bulk and surface formation calculations, which should give more accurate estimation of lattice parameters.¹¹⁻¹³ Wavefunctions were converged to within 10^{-8} eV and forces were computed using a fast Fourier transform (FFT) grid; the maximum force on each atom was converged to < 0.01 eV \AA^{-1} . The unit cells of bulk Ni (space group $Fm\bar{3}m$),¹⁴ Ni₂P (space group $P\bar{6}2m$),¹⁵ and Ni₁₂P₅ (space group $I4/m$)¹⁵ were built based on crystallographic data, and the lattice parameters were then optimized using DFT. Calculations of bulk Ni, Ni₁₂P₅, and Ni₂P were computed using a Γ -centered $7 \times 7 \times 7$ and $8 \times 8 \times 14$ sampling of the Brillouin zone (k-point meshes), respectively.¹⁶ Energy convergence tests were performed to ensure adequate k-point mesh sizes were used; energies changed by less than 3×10^{-3} eV when the k-point mesh was increased to $9 \times 9 \times 9$ for Ni and $16 \times 16 \times 28$ for Ni₁₂P₅ and Ni₂P (Figure S28). The optimized bulk lattice parameters for Ni ($a = b = c = 3.52$ \AA), Ni₂P ($a = b = 5.87$ \AA , $c = 3.37$ \AA) and Ni₁₂P₅ ($a = b = 8.63$ \AA , $c = 5.07$ \AA) were consistent with previous DFT studies¹⁷ and in close agreement with the measured

values ($a = b = c = 3.52 \text{ \AA}$),¹⁴ ($a = b = 5.86 \text{ \AA}$, $c = 3.38 \text{ \AA}$),¹⁸ and ($a = b = 8.65 \text{ \AA}$, $c = 5.07 \text{ \AA}$).¹⁸ All Ni calculations were run spin-polarized because of its ferromagnetic properties. Calculations showed less than 10^{-4} eV energy difference between spin- and non-spin polarized calculations for $\text{Ni}_{12}\text{P}_5(001)$ and $\text{Ni}_2\text{P}(001)$ calculations, consistent with previous DFT studies,¹⁷ so all calculations of $\text{Ni}_{12}\text{P}_5(001)$ and $\text{Ni}_2\text{P}(001)$ surfaces were done without spin-polarization.

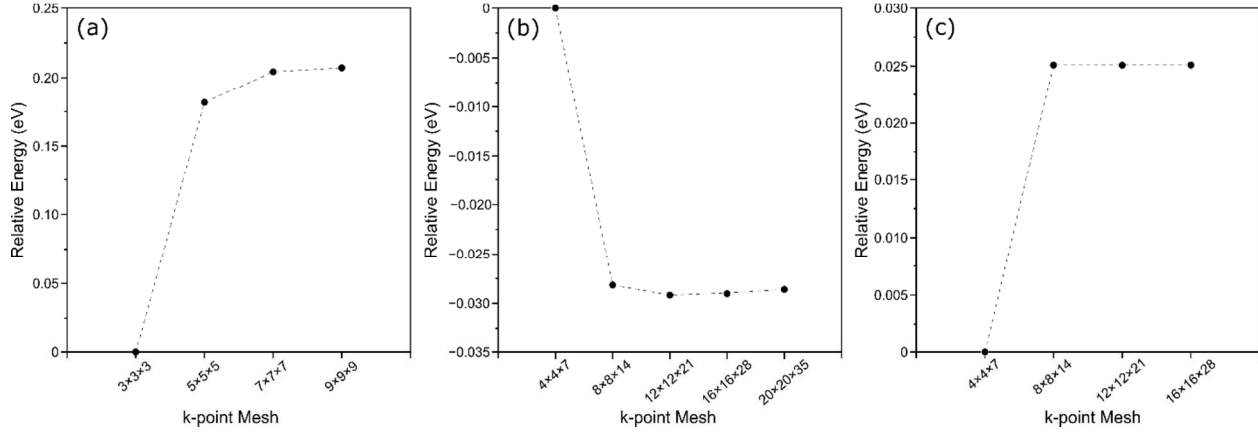


Figure S28. k-point convergence test for bulk Ni (a), Ni_2P (b), and Ni_{12}P_5 (c).

Optimized bulk structures were cleaved along different Miller indices and the surface formation energy was calculated by

$$E = \left(E_{\text{surf}} - \frac{N_{\text{surf}}}{N_{\text{bulk}}} E_{\text{bulk}} \right) \frac{1}{2A} \quad (\text{S11})$$

where N is the number of atoms and A is the area of the surface. The closed-packed Ni(111) surface has the lowest surface formation energy ($1008 \text{ kJ mol}^{-1} \text{ nm}^{-2}$) compared to Ni(100) ($1142 \text{ kJ mol}^{-1} \text{ nm}^{-2}$) and Ni(110) ($1211 \text{ kJ mol}^{-1} \text{ nm}^{-2}$) (Fig. S29a), as well-established for transition metals.¹⁹ For Ni_2P and Ni_{12}P_5 surfaces, there is an alternation of planes in the z -direction that have different Ni and P composition; scanning tunneling microscope (STM) images confirm the existence of two different terminations on $\text{Ni}_2\text{P}(001)$ single crystals.²⁰ DFT calculations indicate that the Ni-rich terminations in $\text{Ni}_2\text{P}(001)$ and $\text{Ni}_{12}\text{P}_5(001)$ have the lowest surface formation energies ($823 \text{ kJ mol}^{-1} \text{ nm}^{-2}$ and $963 \text{ kJ mol}^{-1} \text{ nm}^{-2}$, respectively) (Fig. S29b and c). Thus, the Ni(111), $\text{Ni}_{12}\text{P}_5(001)$, and $\text{Ni}_2\text{P}(001)$ surfaces were used, although the kinetic relevance of other surfaces cannot be eliminated. These surfaces were modeled with k -point meshes of $4 \times 4 \times 1$ and $5 \times 5 \times 1$ for Ni(111), $\text{Ni}_{12}\text{P}_5(001)$, and $\text{Ni}_2\text{P}(001)$ surfaces, respectively, and the energies changed by less than 1×10^{-2} eV if a larger k -point meshes were used (Fig. S30).

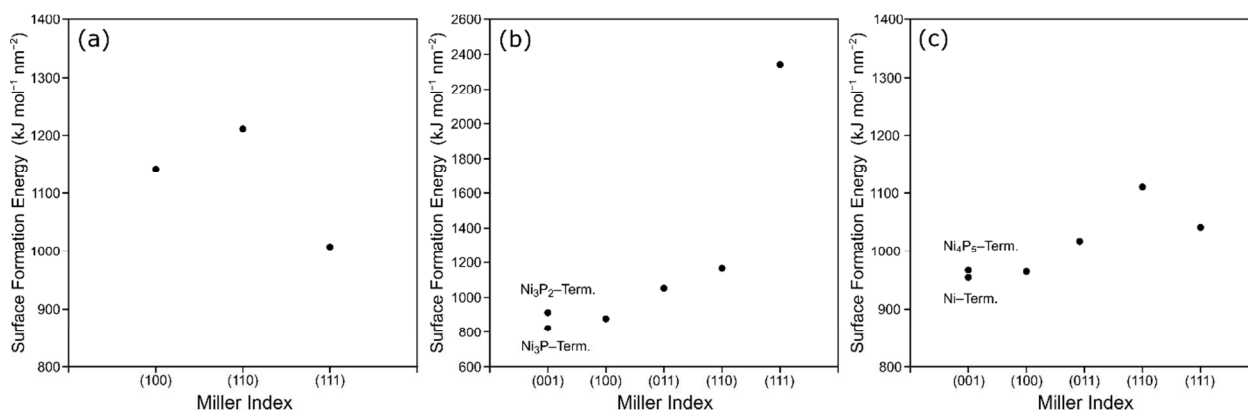


Figure S29. Surface formation energies for Ni (a), Ni₂P (b), and Ni₁₂P₅ (c).

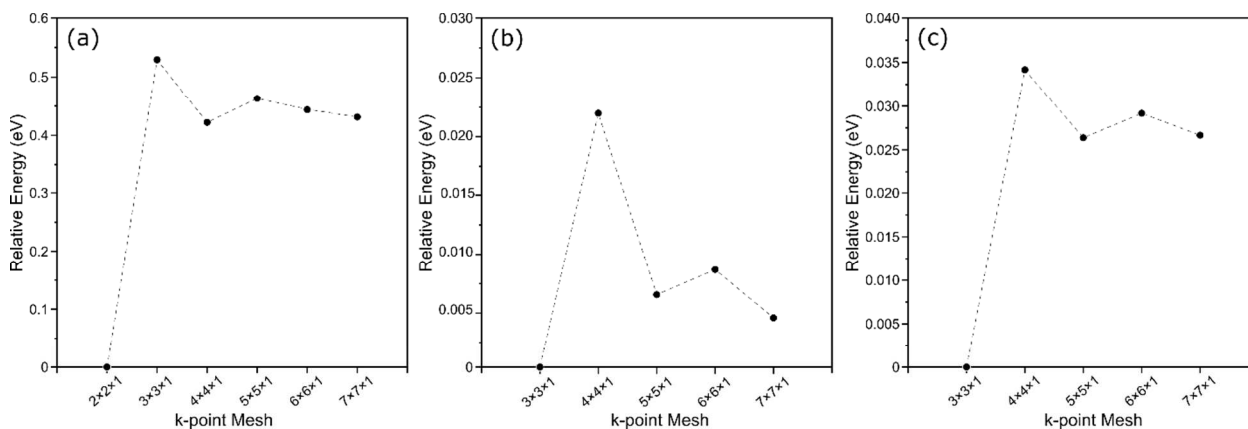


Figure S30. k-point convergence test for Ni(111) (a), Ni₂P(001) (b), and Ni₁₂P₅(001) (c).

S3.3.2. Energy Barrier Calculations

The revised Perdew–Burke–Ernzerhof (RPBE) functional was used for calculations of adsorption, reaction, and activation energies because it exhibits better performance in predicting adsorption energies in metal surfaces.^{11–13} Calculations discussed in Sections 2.3 and 2.4 were performed using optB88-vdW,²¹ optB86b-vdW,²² RPBE-D3BJ,²³ and vdW-DF2²⁴ functionals which attempt to include dispersion interactions such as van der Waals forces. Wavefunctions were converged to within 10⁻⁶ eV and structures were relaxed until all forces on unconstrained atoms were < 0.05 eVÅ⁻¹. Gaseous species were modeled within 16 × 16 × 16 Å unit cells of vacuum. The Ni(111) catalyst surface was modeled as a 3 × 3 closed-packed periodic lattice with four layers in the orthogonal direction and a 10 Å vacuum between slabs (Fig. S27a); the bottom two layers were fixed in their bulk positions and the top two layers relaxed. After geometric convergence, a single-point calculation with a (8 × 8 × 1) *k*-point mesh was performed to determine the electronic energy. The Ni₂P(001) and Ni₁₂P₅(001) surfaces shown in Figure S31 were modeled with two repeating units and a 10 Å vacuum in the *z*-direction. The bottom repeat units (two atomic layers for Ni₂P and four atomic layers for Ni₁₂P₅, Figures S31b and c) were fixed in their bulk positions while all other atoms were relaxed.

Transition state structures were obtained for each elementary reaction by using the nudged elastic band (NEB) method^{25,26} and the dimer method.²⁷ The NEB method was carried out using 16 images, and

wavefunctions were converged to within 10^{-4} eV. The maximum force on each atom was converged to <0.5 eV \AA^{-1} . These protocols provided an estimate of the reaction path and starting points for the structure and the reactive mode for each transition state. The dimer algorithm was then used with wavefunctions converged to within 10^{-6} eV, and the maximum force on each atom was converged to <0.05 eV \AA^{-1} .

Frequency calculations were performed on gas phase molecules and all optimized adsorbed species (all catalyst atoms were fixed) to determine zero-point vibrational energies (ZPVE), and vibrational, translational and rotational enthalpy and free energy. These terms were then used, together with electronic energies (E_0 , provided by VASP), to estimate enthalpies:

$$H = E_0 + ZPVE + H_{vib} + H_{trans} + H_{rot} \quad (\text{S12})$$

and free energies:

$$G = G_0 + ZPVE + G_{vib} + G_{trans} + G_{rot} \quad (\text{S13})$$

for all reactants, products, and transition states at 543 K. For calculations which include a periodic surface, there are no translational or rotational degrees of freedom and DFT-derived vibrational frequencies can be used to determine the ZPVE, H_{vib} , and G_{vib} .²⁸

$$ZPVE = \sum_i (\frac{1}{2} v_i h) \quad (\text{S14})$$

$$H_{vib} = \sum_i \left(\frac{v_i h e^{-\frac{v_i h}{kT}}}{1 - e^{-\frac{v_i h}{kT}}} \right) \quad (\text{S15})$$

$$G_{vib} = \sum_i \left(-kT \ln \frac{1}{1 - e^{-\frac{v_i h}{kT}}} \right) \quad (\text{S16})$$

For gaseous molecules, translational and rotational enthalpies and free energies were also computed from statistical mechanics:

$$H_{trans} = \frac{5}{2} kT \quad (\text{S17})$$

$$H_{rot,linear} = kT \quad (\text{S18})$$

$$H_{rot,nonlinear} = \frac{3}{2} kT \quad (\text{S19})$$

$$G_{trans} = -kT \ln \left[\left(\frac{2\pi M kT}{h^2} \right)^{3/2} V \right] \quad (\text{S20})$$

$$G_{rot} = -kT \ln \left[\frac{\pi^{1/2}}{\sigma} \left(\frac{T^3}{\theta_x \theta_y \theta_z} \right)^{1/2} \right] \quad (\text{S21})$$

$$\theta_i = \frac{h^2}{8\pi^2 I_i k} \quad (\text{S22})$$

where I_i is the moment of inertia about axes x, y or z and σ is the symmetry number of the molecule. DFT-derived intrinsic enthalpy and free energy barriers (ΔH_{act} and ΔG_{act} , respectively) and reaction energies (ΔH_{rxn} or ΔG_{rxn}) denote differences between a transition state or the product and the precursor reactant for that elementary step. Overall barriers (ΔH^\ddagger and ΔG^\ddagger) are defined as the enthalpy or free energy of forming the partially-dehydrogenated transition state [$\text{C}_5\text{H}_{(10-\lambda/2)}\text{O}^{**} \ddagger$] and a stoichiometric amount of gas-phase H_2 from gas-phase MTHF ($\text{C}_5\text{H}_{10}\text{O}$) and a bare surface.

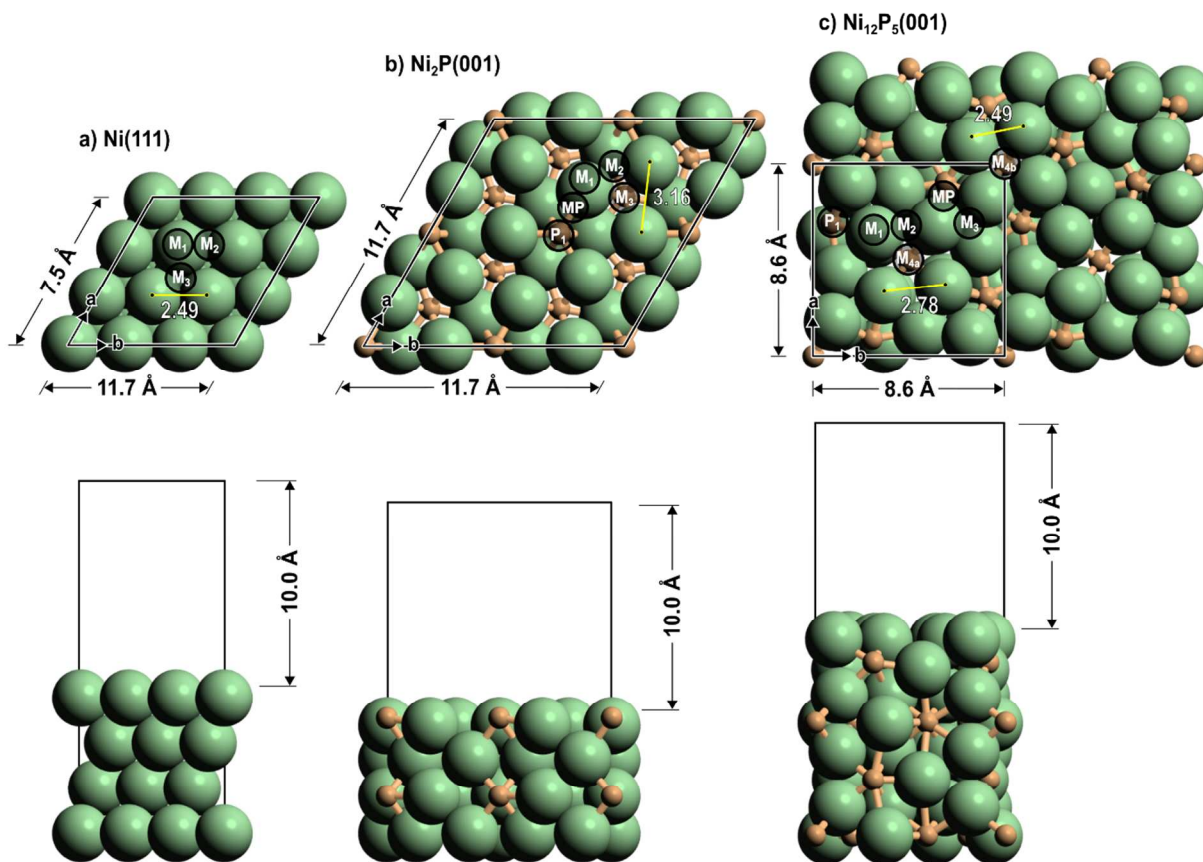


Figure S31. Top and side views of Ni (a) Ni_2P (b) and Ni_{12}P_5 (c) supercells. The adsorption sites are labeled by M_1 : metal atop, M_2 : metal bridge, M_3 : metal 3-fold hollow, M_4 : metal 4-fold hollow, MP : metal-phosphorus bridge, and P_1 : phosphorus atop. The bottom two layers for Ni and the bottom repeat units for Ni_{12}P_5 and Ni_2P (two atomic layers for Ni_2P and four atomic layers for Ni_{12}P_5) were fixed in their bulk.

S4. Derivation for Measured Equilibrium Constant for Dehydrogenation of MTHF to MF

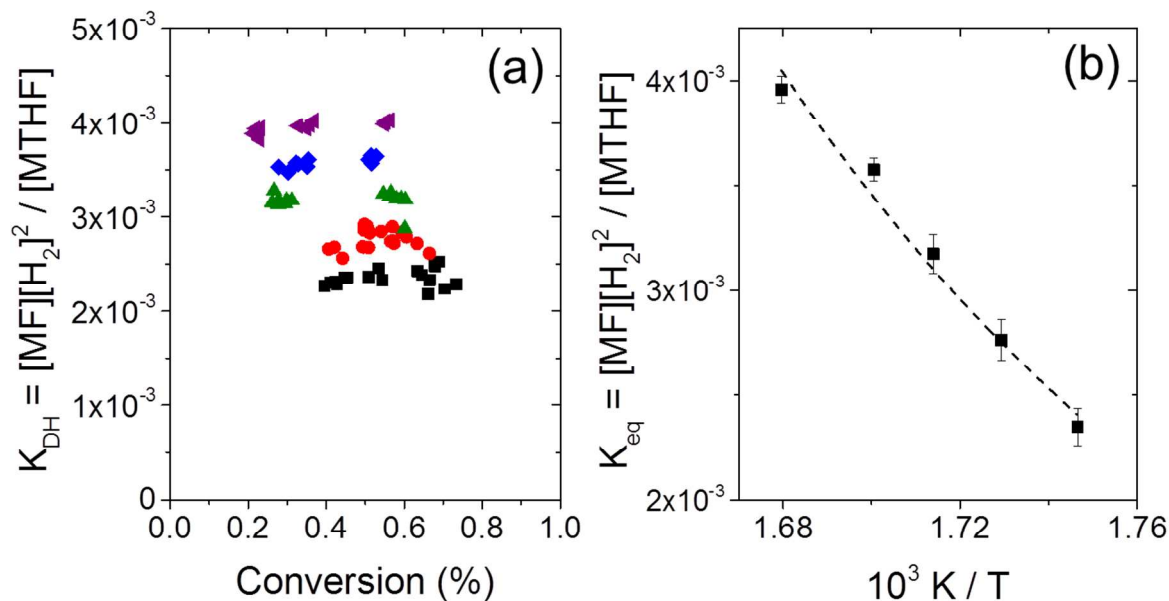


Figure S32. (a) Measured ratio of MF, H₂, and MTHF over a range of conversions with feed composition 5 kPa MTHF and 0.125 MPa H₂ at 593 K (◀), 588 K (◆), 583 K (▲), 578 K (●), and 573 K (■) over Ni₂P. (b) Average ratio measured MF, H₂, and MTHF which indicate equilibrium constant (K_{DH}) for dehydrogenation of MTHF to MF as a function of temperature in 5 kPa MTHF and 0.125 MPa H₂ over Ni₂P. Trend line indicates exponential fit.

Tabulated values for equilibrium constant for MTHF dehydrogenation to MF, K_{DH} , and free energy, ΔG_{DH} , were inconsistent with experimental results. To experimentally measure ΔG_{DH} and K_{DH} , the ratio of 2-methylfuran (MF), hydrogen (H₂), and 2-methyltetrahydrofuran (MTHF) pressures were measured over a range of residence times (i.e., conversions) and temperatures (573-593 K) over Ni₂P (Figure S32a). The ratio of MF, H₂, and MTHF pressures ($\frac{[H_2]^2[C_5H_6O]}{[C_5H_{10}O]}$) was constant within this range of conversions representative of conditions during kinetic measurements, which indicates that dehydrogenation of MTHF and hydrogenation of MF have reached equilibrium ($\eta = 1$) at these conversions; therefore, this ratio is equivalent to K_{DH} based on Equations S23 and S24:

$$K_{DH} = \frac{[H_2]^2[C_5H_6O]}{[C_5H_{10}O]} \quad (S23)$$

ΔG_{DH} was then calculated from the exponential fit of the Eyring-Polanyi plot of the measured K_{DH} values (Figure S32b),

$$K_{DH} = e^{-\Delta G_{DH}/RT} \quad (S24)$$

where R is the universal gas constant and T is the temperature.

S5. Error analysis

S5.1. Sources of Error

S5.1.1. Instrumentation: Sources of Random Error and Preventative Measures

Table S6 indicates the error of each instrument as reported by the manufacturer. Mass flow controllers (MFCs) are calibrated weekly using a bubble meter at the outlet of the GC. The system is leak checked weekly, and the leak rate must be less than 5 ml min⁻¹ at the highest pressure (~800 psig). The electronic pressure controller is calibrated every 3 months using the digital pressure gauge upstream of the reactor. Calibrations for the pressure controller are done at ~20 ml min⁻¹ to avoid effects of pressure drop throughout the system. The digital pressure gauge is compared with the delivery pressure on the H₂ tank regulator weekly. The furnace PID controller is programmed to automatically adjust the tuning parameters during experiments. Measurements taken at temperatures outside of ±0.2°C of the set point (measured by the thermocouple submerged within the catalyst bed) are manually rejected. Sensitivity factors for hydrocarbons and oxygenates were calibrated relative to 2-methyltetrahydrofuran (MTHF), and are adjusted when the MTHF sensitivity factor is recalibrated weekly during by-pass measurements. Error from each instrument propagates through to reported rate measurements.

Table S6. Error reported by equipment manufacturer

Equipment	Controlled or Measured Variable	Error Reported by Manufacturer
Parker-Porter Mass Flow Controller	Gas flow rates (H ₂ , NH ₃ , CO)	± 1% of full scale
Teledyne-Isco stainless-steel syringe pump	MTHF flow rate	± 0.5 % of set point
Watlow Furnace PID Controller	Reactor temperature	± 0.2°C
Omega Digital Pressure Gauge	Pressure upstream of reactor	±0.25% Full scale (1000 psig)
Equilibar Electronic pressure controller	Pressure downstream of reactor	±0.25% Full scale (1000 psig)
Agilent HP 6890 Gas chromatograph	Effluent composition	± 1% relative standard deviation
Mass balance	Mass of catalyst	± 1 mg

Overall repeatability within the system is measured weekly with by-pass measurements. The fluctuations in the MFCs, syringe pump, and GC all contribute to the measured error. During experiments, the carbon and oxygen balances indicate if the relative syringe pump and MFC flow rates are accurate. These two mole balances must close within 10% for any measured value to be considered. The combined uncertainty of the GC, MFCs, and syringe pump measured through the by-pass is typically between 5-10%. The follow sections will compare the measured random error with the calculated propagated error from the instruments.

S5.1.2. Sources of Systematic Error

Systematic uncertainty results from deviation in thermocouple calibration and the broad distribution in cluster size (Figure S20-S24). The reactor temperature is controlled with the Watlow PID controller, but the reported temperature is measured by a thermocouple co-axially aligned with the reactor and submerged in the catalyst bed for a more accurate temperature measurement, as opposed to using the thermocouples embedded in the furnace walls. The thermocouple was initially calibrated at 0°C and room

temperature. If the thermocouple has slowly drifted, then all reported temperatures and rates would systematically be off, but this would not result in fluctuations between measurements.

Similarly, the cluster size distribution for each catalyst affects the uncertainty in the calculated residence time and turnover rates. A certain mass of catalyst is used when measuring a specific data set (e.g., MTHF pressure or temperature dependence) and the number of active sites is held constant during that particular data set (excluding effects of deactivation discussed in the following section). Changing the number of active sites would change the magnitude of the reported rates, but all the rates within that data set be adjusted by the same factor. Values we report to determine the kinetic model and active site properties (i.e., rate dependencies and activation enthalpies) are not affected by the magnitude of the rates, but rather the change in the rates as a function of pressure or temperature; therefore, the systematic error resulting from drift in thermocouple calibration and cluster size distribution will not cause fluctuations between measurements and are not reported in the calculated error.

S5.2. Procedure for Data Collection and Fitting

S5.2.1. Steady-State Measurements: Accounting for Deactivation and Repeatability

For every condition, 4-5 measurements are taken at ~30 min intervals. The system takes roughly 1 hour to reach steady state. The carbon and oxygen balances are used to determine if the system has reached steady state. Within each data set (e.g., MTHF or temperature dependence) a reference condition is measured at least twice to account for deactivation (loss of active sites) over time. Catalyst is replaced if the selectivity (χ) changes more than 10%, as this indicates a change in the catalyst structure not just loss of active sites.

For any data sets taken without CO or NH₃, each pressure is measured at least 3 space velocities to report rates extrapolated to 0% conversion. For data sets taken with CO and NH₃, rates are measured at a single space velocity for each pressure. Temperature dependence measurements are taken in increasing order of temperature after initial measuring the rates at 543 K. After measuring the rate at the highest temperature, the final rate measurement is taken at 543 K to correct for deactivation during the data collection.

S5.2.2. Appropriate Weighting Methods in Origin

Origin provides three different weighting methods for non-linear curve fits, and adjusts the fitting parameters (e.g., a and b for a power law fit, $y = a \cdot x^b$) to reduce χ^2 given the following equation

$$\chi^2 = \sum_i^n w_i [Y_i - f(x_i; \hat{\theta})]^2$$

Here, w_i is the weight of each data point, Y_i is the magnitude of the value, and $f(x_i; \hat{\theta})$ is the y-value of the fitted function at x_i for data point i . Table S7 describes the different weighting methods available in Origin. Previous reported results used the Statistical weighting method, which normalizes weights by the magnitude of the y-value. This weighting method does not account for the error within each measurement. Weighting values equally (No Weights method) causes the fit to be skewed towards higher values. The Instrumental weighting method uses a user defined standard deviation (σ_i) to calculate w_i , so values with more error carry less weight in the fit.

Table S7. Weighting Methods in OriginPro

Weighting Method	Weight, w_i	Results
No Weights	1	Fit is weighted towards higher values
Statistical	$1/y_i$	Normalizes weight by magnitude of value (y_i)
Instrumental	$1/\sigma_i^2$	Adjusts fit to user defined standard deviation (σ_i), most accurate method

The following section compares the measured standard deviation with the calculated standard deviation using error propagation of the instrument uncertainty from Section S5.1.

S5.3. Error Propagation Calculations

Here the standard deviation of reported rates are described for the MTHF pressure dependence and temperature dependence based on error propagation from each source of random error listed in Section S5.1, and compared with the standard deviation calculated by the fits within Origin.

Molar Flow Rates

The standard deviation of molar flowrates \dot{n} for each reactant (MTHF, H₂, CO, and NH₃) are calculated below:

$$n_{MTHF} = \dot{V} * \rho / MW$$

$$\sigma_{n,MTHF} = \dot{V} * 0.5\% * \rho / MW$$

Here, \dot{V} is the volumetric flow rate set on the syringe pump, ρ is the density of MTHF, and MW is the molecular weight of MTHF.

$$n_{H_2} = (\dot{V}_1 + \dot{V}_2 * 99\%) * P_{atm} / RT$$

$$\sigma_{n,H_2} = \sqrt{(1\% * 500sccm)^2 + (1\% * 300sccm * 99\%)^2} * P_{atm} / RT$$

Here, \dot{V}_1 and \dot{V}_2 are the volumetric flowrates in standard cubic centimeters per minute (sccm) through the MFCs, R is the universal gas constant, T is 298 K, and P_{atm} is 1 atm. A mixture of 1% CO in H₂ is used to co-feed CO, meaning both MFCs of different full scales are used to feed H₂ during experiments when CO is co-fed. The volumetric flow rate and error attributed to the co-fed MFC are multiplied by 99% to only account for the H₂. Standard deviation in CO and NH₃ flowrates are calculated similarly below:

$$n_{CO} = (\dot{V}_2) * \frac{P_{atm}}{RT} * 1\% \text{ CO in } H_2$$

$$\sigma_{n,CO} = \sqrt{(1\% * 300sccm)^2} * \frac{P_{atm}}{RT} * 1\%$$

$$n_{NH_3} = (\dot{V}) * \frac{P_{atm}}{RT}$$

$$\sigma_{n,NH_3} = \sqrt{(1\% * 300sccm)^2} * \frac{P_{atm}}{RT}$$

Reactant Pressures

Error in reactant pressure, $\sigma_{P,i}$, is a function of the molar flowrates and the total system pressure, P_{total} , controlled by the electronic pressure controller, where $\sigma_{P,total} = 0.25\% * 1000psi$.

$$P_i = \frac{\dot{n}_i}{n_{MTHF} + \dot{n}_{H_2} + \dot{n}_{CO} + \dot{n}_{NH_3}} * P_{Total}$$

$$\sigma_{P,i} = \sqrt{\left(\frac{\sigma_{n,i}}{\dot{n}_i}\right)^2 + \left(\frac{\sigma_{n,total}}{\dot{n}_{total}}\right)^2 + \left(\frac{\sigma_{P,total}}{P_{Total}}\right)^2} * P_i$$

Here $\sigma_{n,i}$, \dot{n}_i , and P_i are the standard deviation of molar flow rate, molar flow rate, and reactant pressure for reactant i, where i is CO, NH₃, MTHF, or H₂. The error in total molar flowrate, $\sigma_{n,total}$, is calculated as the sum of squares of standard deviation for each reactant:

$$\sigma_{n,total} = \sqrt{(\sigma_{n,MTHF})^2 + (\sigma_{n,H2})^2 + (\sigma_{n,CO})^2 + (\sigma_{n,NH3})^2}$$

Conversion

The standard deviation in conversion, σ_X , is a function of the sensitivity factors and partial pressures each product, j, and initial pressure of MTHF, $P_{0,MTHF}$.

$$X = \frac{\sum(P_j * C_j)}{P_{0,MTHF} * 5}$$

Here, conversion, X, is reported on a carbon basis relative to the initial carbon in MTHF ($P_{0,MTHF} * 5$, as MTHF contains 5 carbons), so C_j is the carbon number for each product, j. GC measurements are taken at atmospheric pressure, so the measured area is converted to an atmospheric partial pressure using the sensitivity factor, then multiplied by the ratio of the total system pressure to atmospheric pressure to calculate the pressure of product j, P_j , within the reactor.

$$P_j = \text{Measured area} * \text{Sensitivity factor} * P_{total}/P_{atm}$$

Agilent listed the uncertainty for GC measurements as $\pm 1\%$ relative standard deviation:

$$\frac{\sigma_{GC}}{\text{Measured area} * \text{Sensitivity factor}} = 1\%$$

Here the error in measured area and sensitivity factor are encompassed in σ_{GC} . The standard error in product partial pressure is given as

$$\sigma_{P,j} = \sqrt{\left(\frac{\sigma_{GC}}{GC \text{ measurement}}\right)^2 + \left(\frac{\sigma_{P,total}}{P_{Total}}\right)^2 * P_j}$$

The calculated standard deviation for all products is

$$\sigma_{\sum P_j * C_j} = \sqrt{\sum_j (\sigma_{P,j} * C_j)^2}$$

Finally, the standard error in conversion is calculated as

$$\sigma_X = \sqrt{\left(\frac{\sigma_{\sum P_j * C_j}}{\sum P_j * C_j}\right)^2 + \left(\frac{\sigma_{P,MTHF}}{P_{0,MTHF}}\right)^2 * X}$$

Turnover Rates for ^xC-O Bond Rupture

Rates are reported as the formation rates of products for each ^xC-O bond rupture pathway.

$$r^{x_{C-O}} = \frac{\sum P_j^{x_{C-O}}}{P_{0,MTHF}} * SV$$

Where the space velocity, SV, is a function of the molar flow rate of MTHF and number of surface sites, $n_{surf,Ni}$ and defined as the following:

$$SV = \frac{n_{MTHF}}{n_{surf,Ni}}$$

$$\sigma_{SV} = \sqrt{\left(\frac{\sigma_{n,MTHF}}{n_{MTHF}}\right)^2 + \left(\frac{\sigma_{n,surf Ni}}{n_{surf,Ni}}\right)^2 * SV}$$

$$\sigma_{n,surf Ni} = \sqrt{\left(\frac{\sigma_{mass}}{mass\ catalyst\ loaded}\right)^2}$$

As discussed in Section 5.1., there is systematic error in the number of surface sites based on the distribution of cluster sizes, but this will not result in fluctuations or random error, and is not included in the standard deviation for SV. The standard deviation for reported rates are calculated as below:

$$\sigma_{r_{x_{C-O}}} = \sqrt{\left(\frac{\sum_j \sigma_{P,j,x_{C-O}}}{\sum P_j x_{C-O}}\right)^2 + \left(\frac{\sigma_{P,MTHF}}{P_{0,MTHF}}\right)^2 + \left(\frac{\sigma_{SV}}{SV}\right)^2 * r_{x_{C-O}}}$$

These calculated standard deviations are used as σ_i in the weighting for the instrumental fits. The regression performed in Origin calculates a fit based on reducing χ^2 as discussed in Section S5.2.2, which calculates the corresponding standard deviation for the reported fit. The fits, and subsequently rate orders, are nominally the same regardless of the standard deviation; therefore, the reported conclusions regarding the kinetic model and proposed mechanism remain the same. Table S8 displays the average, minimum, and maximum standard deviations based on the measured and calculated values for the MTHF pressure dependence. The measured error is greater than the error calculated through propagation of standard deviations, and therefore, may be a more accurate representation of the precision of measurements at each condition because it incorporates any error unaccounted for in the system.

Table S8 Measured and calculated uncertainties for MTHF Dependence (5 kPa CO, 0.5 MPa H₂, 543 K 19 nm Ni₁₂P₅)

C-O bond rupture pathway	Measured Error, % ($\sigma_i / r_{x_{C-O}}$)			Calculated Error, % ($\sigma_i / r_{x_{C-O}}$)		
	Average	Minimum	Maximum	Average	Minimum	Maximum
³ C-O	8.6%	0.9%	26.0%	6.7%	5.4%	9.7%
² C-O	13.6%	0.5%	45.6%	6.9%	5.5%	9.8%

Rates Extrapolated to 0% Conversion

For data sets taken without co-fed CO or NH₃ (i.e., when rates decrease a function of conversion due to product inhibition), rates are measured at multiple space velocities and the reported rate is at 0% conversion. Rates for both ^xC-O bond rupture pathways, $r_{x_{C-O}}$, are plotted against X with x and y error bars (σ_X and $\sigma_{r_{x_{C-O}}}$, respectively) for each individual temperature or pressure and a linear regression is performed in Origin to obtain the following equation:

$$r_{x_{C-O}} = m_{x_{C-O}}X + b_{x_{C-O}}$$

where $m_{x_{C-O}}$ and $b_{x_{C-O}}$ are the slope and intercept for the respective ^xC-O bond rupture pathway. The intercept represents the rate at 0% conversion, which is used for to determine the rate order for pressure dependences and activation enthalpies when CO or NH₃ are not co-fed. The error in $b_{x_{C-O}}$ is calculated through a series of steps below rather than using the standard error in $b_{x_{C-O}}$ calculated by Origin, which was used for previously reported values. The standard deviation of the slope is calculated as

$$\sigma_{m_{x_{C-O}}} = \sqrt{\frac{\frac{1}{N-2} \sum_i^N (r_{x_{C-O}} - \widehat{r_{x_{C-O}}})^2}{\sum_i^N (X_i - \bar{X})^2}}$$

Here, N is the number of measurements taken at the given temperature or pressure; $r_{x_{C-O}}$ is the measured rate at the measured conversion, X_i ; $\widehat{r_{x_{C-O}}}$ is the calculated rate at X_i using the linear regression; and \bar{X} is the average conversion at the specific space velocity. Solving the linear fit for $b_{x_{C-O}}$ gives

$$b_{x_{C-O}} = r_{x_{C-O}} - m_{x_{C-O}} X$$

And the standard error of $b_{x_{C-O}}$ is then

$$\sigma_{b_{x_{C-O}}} = \sqrt{(\sigma_{r_{x_{C-O}}})^2 + (\sigma_{m_{x_{C-O}}})^2}$$

Where $\sigma_{m_{x_{C-O}}}$ is the standard deviation for the product of $m_{x_{C-O}}$ and X , defined as

$$\sigma_{m_{x_{C-O}}} = \sqrt{\left(\frac{\sigma_{m_{x_{C-O}}}}{m_{x_{C-O}}}\right)^2 + \left(\frac{\sigma_X}{X}\right)^2 * m_{x_{C-O}} X}$$

The reported rates at each condition (i.e., pressure or temperature) are $b_{x_{C-O}} \pm \sigma_{b_{x_{C-O}}}$.

Transition State Equilibrium Constant

For enthalpic measurements, the plotted transition state equilibrium constant, K^\ddagger , derived from Transition State Theory is calculated as a function of the initial H_2 and MTHF pressures (P_{0,H_2} and $P_{0,MTHF}$, respectively), temperature (T) in K, and measured rates for $^x C-O$ bond rupture,

$$K^\ddagger = r_{x_{C-O}} \frac{P_{0,H_2}^m}{T * P_{0,MTHF}}$$

Here P_{0,H_2}^m is the inlet pressure of H_2 raised to the m power, where m is the magnitude of the rate dependence on H_2 pressure for $^x C-O$ bond rupture (i.e., $1/2$ for $^3 C-O$ bond rupture and 1 for $^2 C-O$ bond rupture). The standard deviation for P_{0,H_2}^m is

$$\sigma_{P_{0,H_2}^m} = m * \frac{\sigma_{P_{0,H_2}}}{P_{0,H_2}}$$

The standard deviation for K^\ddagger is defined as

$$\sigma_{K^\ddagger} = \sqrt{\left(\frac{\sigma_{r_{x_{C-O}}}}{r_{x_{C-O}}}\right)^2 + \left(\frac{\sigma_T}{T}\right)^2 + \left(\frac{\sigma_{P_{0,MTHF}}}{P_{0,MTHF}}\right)^2 + \left(\frac{\sigma_{P_{0,H_2}^m}}{P_{0,H_2}^m}\right)^2 * K^\ddagger}$$

Where σ_T is 0.2 K. In the example temperature dependence data for a clean surface, rates are reported at 0% conversion; therefore, $b_{x_{C-O}}$ and $\sigma_{b_{x_{C-O}}}$ are used in place of $r_{x_{C-O}}$ and $\sigma_{r_{x_{C-O}}}$.

Activation Enthalpy

Activation enthalpies, ΔH^\ddagger , are extracted from an exponential fit of K^\ddagger on an Eyring-Polanyi plot, as K^\ddagger is defined as

$$K^\ddagger = e^{-\Delta G^\ddagger/RT}$$

ΔG^\ddagger is expanded to give

$$K^\ddagger = e^{-\Delta H^\ddagger/RT} * e^{\Delta S^\ddagger/R}$$

ΔH^\ddagger is calculated from the slope of an exponential fit to $y = Ae^{Bx}$, where y is K^\ddagger , and x is $1000/T$ using Origin. Rearranging the above equation to solve for ΔH^\ddagger results as

$$\Delta H^\ddagger = \frac{\ln(K^\ddagger)}{\Delta S^\ddagger} * T$$

The standard deviation for ΔH^\ddagger is dependent on σ_{K^\ddagger} and σ_T

$$\sigma_{\Delta H^\ddagger} = \sqrt{\left(\frac{\sigma_{\ln K^\ddagger}}{\ln(K^\ddagger)}\right)^2 + \left(\frac{\sigma_T}{T}\right)^2} * \Delta H^\ddagger$$

Where $\sigma_{\ln K^\ddagger}$ is defined as

$$\sigma_{\ln K^\ddagger} = \frac{\sigma_{K^\ddagger}}{K^\ddagger}$$

ΔS^\ddagger is dependent on K^\ddagger so the standard deviation in ΔS^\ddagger is not included in calculation for $\sigma_{\Delta H^\ddagger}$. The activation enthalpies are effectively equivalent regardless if $\sigma_{b_{x_{c-o}}}$ is determined from the error in the intercept calculated by Origin or from the propagated error.

References

- (1) Jiao, L.; Regalbuto, J. R. The synthesis of highly dispersed noble and base metals on silica via strong electrostatic adsorption: I. Amorphous silica. *J. Catal.* **2008**, *260*, 329-341.
- (2) Wu, S. K.; Lai, P. C.; Lin, Y. C. Atmospheric hydrodeoxygenation of guaiacol over nickel phosphide catalysts: Effect of phosphorus composition. *Catal. Lett.* **2014**, *144*, 878-889.
- (3) Cecilia, J. A.; Infantes-Molina, A.; Rodriguez-Castellon, E.; Jimenez-Lopez, A.; Oyama, S. T. Oxygen-removal of dibenzofuran as a model compound in biomass derived bio-oil on nickel phosphide catalysts: Role of phosphorus. *Appl. Catal. B-Environ.* **2013**, *136*, 140-149.
- (4) Moteki, T.; Flaherty, D. W. Mechanistic Insight to C-C bond formation and predictive models for cascade reactions among alcohols on Ca- and Sr-Hydroxyapatites. *ACS Catal.* **2016**, *6*, 4170-4183.
- (5) Kresse, G.; Furthmuller, J. Efficiency of ab-initio total energy calculations for metals and semiconductors using a plane-wave basis set. *Comp. Mater. Sci.* **1996**, *6*, 15-50.
- (6) Kresse, G.; Furthmuller, J. Efficient iterative schemes for ab initio total-energy calculations using a plane-wave basis set. *Phys. Rev. B* **1996**, *54*, 11169-11186.
- (7) Kresse, G.; Hafner, J. Ab-initio molecular-dynamics for open-shell transition-metals. *Phys. Rev. B* **1993**, *48*, 13115-13118.
- (8) Kresse, G.; Hafner, J. Ab-initio molecular-dynamics simulation of the liquid-metal amorphous-semiconductor transition in germanium *Phys. Rev. B* **1994**, *49*, 14251-14269.
- (9) Blochl, P. E. Projector augmented-wave method. *Phys. Rev. B* **1994**, *50*, 17953-17979.
- (10) Kresse, G.; Joubert, D. From ultrasoft pseudopotentials to the projector augmented-wave method. *Phys. Rev. B* **1999**, *59*, 1758-1775.
- (11) Hammer, B.; Hansen, L. B.; Norskov, J. K. Improved adsorption energetics within density-functional theory using revised Perdew-Burke-Ernzerhof functionals. *Phys. Rev. B* **1999**, *59*, 7413-7421.

- (12) Perdew, J. P.; Burke, K.; Ernzerhof, M. Generalized gradient approximation made simple. *Phys. Rev. Lett.* **1996**, *77*, 3865-3868.
- (13) Zhang, Y. K.; Yang, W. T. Comment on "Generalized gradient approximation made simple." *Phys. Rev. Lett.* **1998**, *80*, 890.
- (14) Taylor, A. Lattice parameters of binary nickel cobalt alloys. *J. I. Met.* **1950**, *77*, 585-594.
- (15) Larsson, E. An X-ray investigation of Ni-P system and crystal structures of NiP and NiP₂. *Ark. Kemi.* **1965**, *23*, 335-365.
- (16) Monkhorst, H. J.; Pack, J. D. Special points for Brillouin-zone integrations. *Phys. Rev. B* **1976**, *13*, 5188-5192.
- (17) Ren, J.; Wang, J.; Li, J.; Li, Y. Density functional theory study on crystal nickel phosphides. *J. Fuel Chem. Techno.* **2007**, *35*, 458-464.
- (18) Rundqvist, S. X-ray investigations of Mn₃P, Mn₂P, and Ni₂P. *Acta Chem. Scand.* **1962**, *16*, 992-998.
- (19) Vitos, L.; Ruban, A. V.; Skriver, H. L.; Kollar, J. The surface energy of metals. *Surf. Sci.* **1998**, *411*, 186-202.
- (20) Moula, M. G.; Suzuki, S.; Chun, W. J.; Otani, S.; Oyama, S. T.; Asakura, K. The first atomic-scale observation of a Ni₂P(0001) single crystal surface. *Chem. Lett.* **2006**, *35*, 90-91.
- (21) Klimes, J.; Bowler, D. R.; Michaelides, A. Van der Waals density functionals applied to solids. *Phys. Rev. B* **2011**, *83*, 195131.
- (22) Langreth, D. C.; Lundqvist, B. I.; Chakarova-Kack, S. D.; Cooper, V. R.; Dion, M.; Hyldgaard, P.; Kelkkanen, A.; Kleis, J.; Kong, L. Z.; Li, S.; Moses, P. G.; Murray, E.; Puzder, A.; Rydberg, H.; Schroder, E.; Thonhauser, T. A density functional for sparse matter. *J. Phys.-Condens. Mat.* **2009**, *21*, 1-15.
- (23) Grimme, S.; Ehrlich, S.; Goerigk, L. Effect of the Damping Function in Dispersion Corrected Density Functional Theory. *J. Comput. Chem.* **2011**, *32*, 1456-1465.
- (24) Wellendorff, J.; Lundgaard, K. T.; Mogelhoff, A.; Petzold, V.; Landis, D. D.; Nørskov, J. K.; Bligaard, T.; Jacobsen, K. W. Density functionals for surface science: Exchange-correlation model development with Bayesian error estimation. *Phys. Rev. B* **2012**, *85*, 235149.
- (25) Henkelman, G.; Jónsson, H. Improved tangent estimate in the nudged elastic band method for finding minimum energy paths and saddle points. *J. Chem. Phys.* **2000**, *113*, 9978-9985.
- (26) Jónsson, H.; Mills, G.; Jacobsen, K. W. Nudged elastic band method for finding minimum energy paths of transitions. In *Classical and Quantum Dynamics in Condensed Phase Simulations*; WORLD SCIENTIFIC: 2011, 385-404.
- (27) Henkelman, G.; Jónsson, H. A dimer method for finding saddle points on high dimensional potential surfaces using only first derivatives. *J. Chem. Phys.* **1999**, *111*, 7010-7022.
- (28) McQuarrie, D. A. *Statistical mechanics*; University Science Books: Sausalito, Calif., 2000.